

The Role of Semilabile Oxygen Atoms for Intercalation Chemistry of the Metal-Ion Battery Polyanion Cathodes

Ivan V. Tereshchenko,^{†,‡} Dmitry A. Aksyonov,[†] Oleg A. Drozhzhin,^{†,‡} Igor A. Presniakov,[‡] Alexey V. Sobolev,[‡] Andriy Zhugayevych,[†] Daniil Striukov,[§] Keith J. Stevenson,[†] Evgeny Antipov,[‡] and Artem M. Abakumov^{*,†}

[†] Skoltech Center for Electrochemical Energy Storage, Skolkovo Institute of Science and Technology, Nobel Street 3, 143026 Moscow, Russian Federation

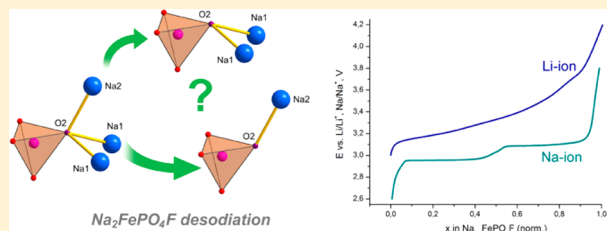
[‡] Department of Chemistry, Lomonosov Moscow State University, 119991 Moscow, Russian Federation

[§] Faculty of Physics, Southern Federal University, 5 Zorge Street, 344090 Rostov-on-Don, Russian Federation

Supporting Information

ABSTRACT: Using the orthorhombic layered $\text{Na}_2\text{FePO}_4\text{F}$ cathode material as a model system we identify the bonding of the alkali metal cations to the semilabile oxygen atoms as an important factor affecting electrochemical activity of alkali cations in polyanion structures. The semilabile oxygens, bonded to the P and alkali cations, but not included into the FeO_4F_2 octahedra, experience severe undercoordination upon alkali cation deintercalation, causing an energy penalty for removing the alkali cations located in the proximity of such semilabile oxygens.

Desodiation of $\text{Na}_2\text{FePO}_4\text{F}$ proceeds through a two-phase mechanism in the Na-ion cell with a formation of an intermediate monoclinic $\text{Na}_{1.55}\text{FePO}_4\text{F}$ phase with coupled $\text{Na}/\text{vacancy}$ and $\text{Fe}^{2+}/\text{Fe}^{3+}$ charge ordering at 50% state of charge. In contrast, desodiation of $\text{Na}_2\text{FePO}_4\text{F}$ in the Li-ion cell demonstrates a sloping charge profile suggesting a solid solution mechanism without formation of a charge-ordered intermediate phase. A combination of a comprehensive crystallographic study and extensive DFT-based calculations demonstrates that the difference in electrochemical behavior of the alkali cation positions is largely related to the different number of the nearest neighbor semilabile oxygen atoms, influencing their desodiation potential and accessibility for the Na/Li chemical exchange, triggering coupled alkali cation–vacancy ordering and $\text{Fe}^{2+}/\text{Fe}^{3+}$ charge ordering, as well as switching between the “solid solution” and “two-phase” charging mechanistic regimes.



INTRODUCTION

The average intercalation potential is one of the key parameters influencing energy density of cathodes (positive electrodes) for metal-ion batteries. Within the same structural environment, the redox potential of the $\text{M}^{n+}/\text{M}^{(n+1)+}$ couple depends on the formal oxidation state of the M cation, its electronegativity and ionization energy, and the details of its electronic configuration.^{1–3} For polyanion cathodes (i.e., comprising the XO_3^{n-} or XO_4^{n-} polyanion groups, such as borates, carbonates, sulfates, phosphates) the anion sublattice plays a decisive role. By changing the X cation in the XO_4^{n-} polyanion group one can adjust the redox potential of the $\text{M}^{n+}/\text{M}^{(n+1)+}$ couple within the same type of polyanionic structure (experimentally demonstrated in the NASICON-type $\text{Li}_x\text{Fe}_2(\text{XO}_4)_3$ structures with X = As, P, Mo, W, S)^{1,4,5} and raise its average potential significantly compared to the redox potential exhibited in oxide structures.⁶ This mechanism, termed an “inductive effect”, is confined to tuning the covalency/ionicity of the M–O bond by varying charge transfer through the M–O–X bond via changing electronegativity of the X cation. According to density functional theory (DFT) computations, the potential of Li^+ deintercalation for the polyanion compounds such as

LiCoXO_4 (X = P, As, Sb), $\text{Li}_2\text{VXO}_4\text{O}$ (X = P, As, Si, Ge), and Li_2MXO_4 (M = Mn, Fe, Co, Ni; X = P, Si, Ge) increases within the row $\text{GeO}_4 < \text{SiO}_4 < \text{SbO}_4 < \text{AsO}_4 < \text{PO}_4$, in almost linear fashion with the X-cation electronegativity.⁷ Increasing the coordination number of the M cation from MO_4 tetrahedral through MO_5 trigonal bipyramidal to MO_6 octahedral environments can also render the M–O bond more ionic and raise the $\text{M}^{n+}/\text{M}^{(n+1)+}$ redox potential, as exemplified by the $\text{Li}_2\text{FeSiO}_4$ – LiFeBO_3 – LiFePO_4 series, demonstrating the potentials of 2.8, 3.0, and 3.5 V, respectively, which correlates well with increasing Fe coordination number from 4 to 6.^{8–11} The connectivity of the coordination polyhedra affects the relative energies of the $\text{M}^{n+}/\text{M}^{(n+1)+}$ redox pairs through electrostatic repulsion depending on the distances between the nearest neighbor cations, which differ significantly if the polyhedra share common corners, edges, or faces. Among other secondary factors influencing the redox properties of the transition metal cations, the proximity of the alkali cation to the redox centers

Received: December 4, 2017

Published: February 23, 2018

can be mentioned, which also affects the M–O bond covalency through a mechanism similar to the inductive effect.¹²

In this article we put forward a conjecture that besides the coordination environment of the transition metal redox centers, the semilabile coordination of the oxygen atoms by neighboring cations must necessarily be taken into account. In a variety of polyanion structures, not all oxygens of the XO_n polyanion groups are directly bonded to the transition metal M cations; the semilabile oxygens are also often present, which are bonded only to the alkali and X cations. Upon alkali cation deintercalation, severe undercoordination of these oxygens arises causing an energy penalty for removing the alkali cations located in the proximity of such semilabile oxygens. We have reported earlier that the semilabile oxygens play a decisive role in antisite disorder upon charge/discharge in Li_2FePO_4F , causing migration of the Fe cations to the Li positions upon charge to compensate for the increasing undercoordination.¹³ One may expect that deintercalation of the alkali cations surrounded by a larger number of semilabile oxygens will be less energetically favorable, which will be reflected in higher deintercalation potential associated with such crystallographic positions. Moreover, the semilabile oxygen atoms carry excessive negative charge and may act as traps for the alkali cations, thus imposing kinetic limitations.^{14,15}

Here, we further support this conjecture by investigation of desodiation of Na_2FePO_4F in both Na-ion and Li-ion cells. This material, first introduced by Ellis et al.,^{16,17} combines several unique characteristics making it a promising cathode for Li-ion and Na-ion batteries. Its structure is built of layers containing face-sharing FeO_4F_2 octahedra, linked through the PO_4 tetrahedral groups. The Na^+ cations are placed in two crystallographically distinct sites between the layers, both exhibiting “6 + 1” mixed oxygen/fluorine coordination. During electrochemical cycling only one Na^+ cation at the A2 (=Na2) position is predominantly mobile, whereas the A1 (=Na1) position can participate only in chemical Na/Li exchange. Although no crystal structures of the charged $Na_{2-x}FePO_4F$ materials are reported so far, Ellis et al.^{14,15} suggested that only the A2 cations were deintercalated during the first charge in the Li-ion cell, ascribing this preference to higher repulsive Fe^{2+} – Na^+ interactions for the A2 site. Later Tripathi et al.¹⁸ calculated the most favorable migration paths for the Na^+ cations using atomistic simulation, concluding that Na can hop between the A1 and A2 sites. Finally, in more recent experimental and computational work Song et al.¹⁹ proposed that the rapid Na–Li exchange can be performed only for the A2 position. To further elucidate structural and electronic changes in this material upon charge/discharge, we perform its structural characterization at different state of charge (SOC) in both Na-ion and Li-ion cells, complementing the experiment with a detailed DFT investigation. In particular, our study demonstrates that the difference in electrochemical behavior of the A1 and A2 positions is largely related to the different number of the nearest neighbor semilabile oxygen atoms that influence their desodiation potential and accessibility for the Na/Li chemical exchange, triggering coupled alkali cation–vacancy ordering and Fe^{2+}/Fe^{3+} charge ordering, as well as switching between the “solid solution” and “two-phase” mechanistic charging regimes.

■ EXPERIMENTAL SECTION

To synthesize the cathode material, 14.5 mmol of $(NH_4)_2Fe(SO_4)_2 \cdot 6H_2O$, 1.8 g of ascorbic acid, and 1.8 g of glucose were dissolved in

distilled water adjusting the volume to 30 mL. Then, 20 mL of 4.6 M sodium hydroxide solution was added to the mixture dropwise under vigorous stirring; ascorbic acid prevented partial oxidation of iron(II) during the alkalization. A 107 mmol amount of sodium fluoride and 25 mL of ethanol were added quickly, and the mixture was rapidly sealed into the Teflon-lined stainless-steel autoclave; the fill factor was 50%. The autoclave was heated to 200 °C and kept at this temperature for 8 h under magnetic stirring. Carefully washed and dried Na_2FePO_4F was carbon-coated using annealing with d-glucose for 2 h at 600 °C under an inert atmosphere.

The phase composition of the samples was characterized by X-ray powder diffraction (XRPD; Huber Guinier camera G670 with an ImagePlate detector, Cu $K\alpha 1$ radiation). The *ex situ* synchrotron X-ray powder diffraction (SXPD) experiments were performed for different SOC at the BM31 beamline of the European Synchrotron Radiation Facility (ESRF, Grenoble). Jana2006 and FullProf software were used for the pattern fitting and Rietveld refinement.^{20–22} *Operando* XRPD data were measured with a Bruker D8 Advance diffractometer (Cu $K\alpha$ radiation, LINXEYE XE linear PSD detector, reflection geometry) in an electrochemical cell with Be X-ray window²³ and with synchrotron X-ray radiation at the BM31 beamline, ESRF ($\lambda = 0.7225 \text{ \AA}$), using an electrochemical cell with sapphire windows.²⁴

The energy-dispersive X-ray (EDX) analysis was performed with a Carl Zeiss NVision 40 scanning microscope equipped with an INCA Energy 350X-Max 80 EDX attachment.

Electrochemical measurements were carried out in two-electrode cells. To form the working electrode, a carbon-coated composite material (Na_2FePO_4F/C) was mixed with conductive carbon black (Timcal Super-P) and polyvinylidene fluoride in 75:15:10 ratio, respectively. The dry mixture was blended with *N*-methyl-2-pyrrolidone. The resulting slurry was applied on Al foil with the “doctor blade” technique and then dried at 75 °C for 3 h. Dried electrodes were rolled, punched to round discs, and dried at 120 °C for 3 h under dynamic vacuum. Electrochemical cells were assembled in an MBraun glovebox under an Ar atmosphere. Three electrolytes were used for the measurements: (a) 1 M $LiPF_6$ in ethylene carbonate and dimethyl carbonate solution with 1:1 volume ratio; (b) 1 M $NaClO_4$ in propylene carbonate + 5% fluoroethylene carbonate; (c) 1 M solution of $LiPF_6$ in sulfolane; the latter was preferable for measurements at an elevated temperature of 75 °C. Metallic Li and Na were used as negative electrodes in the Li-ion and Na-ion cells, respectively. For electrochemical data collection the potentiostat-galvanostat Biologic VMP-3 (EC-Lab software) and Elins P-20X8 (ES8 software) were used. Galvanostatic cycling of the cells was performed between 2.2 and 4.2 V vs Li/Li⁺ and between 2.0 and 3.8 V vs Na/Na⁺ at C/10 rate. The same current density was used to obtain the electrodes at different SOC, unless stated otherwise.

⁵⁷Fe Mössbauer spectra were measured with a constant acceleration MS-1104Em spectrometer. The spectra were treated with the SpectrRelax software.²⁵ The isomer shifts were calibrated with respect to α -Fe at room temperature.

■ DFT CALCULATIONS

Total energies and optimized geometries were calculated with the Vienna Ab Initio Simulation Package (VASP), which implements widely established DFT.^{26–28} The Perdew–Burke–Ernzerhof (PBE) flavor of the generalized gradient approximation (GGA) and projected augmented wave (PAW) method were employed.^{29,30} The standard library potentials “Fe” (3d and 4s valence states), “F”, “O”, “Na”, and “Li” were used. To take into account the strongly correlated character of the d-electrons of Fe, a Hubbard-like correction is added within the Dudarev scheme and U value of 4 eV.^{31,32} To ensure the convergence of wave functions to ground state, the U -ramping approach is employed.³³ All calculations were performed with spin polarization with the ferromagnetic ground state and tetrahedron method with Blöchl corrections for partial occupancies. The convergence study showed that the energy

cutoff of 400 eV and k-point grid of $5 \times 2 \times 2$ are sufficient for reliable description of lattice constants and formation energies. To eliminate the influence of Pulay error, the equilibrium lattice constants were obtained by optimizing the cell shape and atomic positions at constant volume for several contracted and expanded cells (7 points), followed by a third-order polynomial fit of the obtained energies. The relaxation was performed until the forces acting on atoms were smaller than 50 meV/Å, which is enough for obtaining total energies within 1 meV/atom precision. For calculating antisite defect formation energies the relaxation proceeded until the maximum forces were less than 10 meV/Å. The initial crystal structure of $\text{Na}_2\text{FePO}_4\text{F}$ with the $Pbcn$ space group was taken from the experiment. The fully charged compounds relevant for charging in a Na-ion cell (NaFePO_4F) were obtained by removing Na atoms from either A1 or A2 sites. The atomic structure of the half-charged $\text{Na}_{1.5}\text{FePO}_4\text{F}$ compound was found by screening all possible configurations after removal of 0.5 Na (15 configurations in total). The lowest energy configuration coincides with that observed in the experiment. To understand the structural transformations during charging in the Li-ion cell, the discharged ($\text{NaLiFePO}_4\text{F}$) and half-charged ($\text{Na}_{0.5}\text{LiFePO}_4\text{F}$) atomic structures were constructed by substituting Na by Li and considering all possible atomic arrangements. In our calculations we did not take into account the effects of positional disorder. In particular, the $\text{Na}_{0.5}\text{LiFePO}_4\text{F}$ structure has a $P2_1/b$ space group, while in the experiment due to disordered locations of Na it has a $Pbcn$ space group. In all cases, after Na removal or substitution, full optimization of the unit cell and atomic positions was performed. To account for the contribution of lattice vibrations to the free energies, the harmonic approximation was employed, as implemented in the PHONOPY code.³⁴ The force constants were calculated using density functional perturbation theory with increased FFT meshes in VASP. By comparing phonon density of states (PHDOS) and thermodynamic properties of 72-atom and 144-atom supercells, it was found that the 72-atom supercell provides reliable results.

The cluster expansion method, such as implemented in the ATAT code, was used to study phase stabilities.³⁵

The activation energies for cation migration were determined using the nudge elastic band (NEB) method as implemented in VASP code using the 144-atom supercell. The error in activation energy due to limited relaxation precision and small polaron–vacancy/cation binding intervention is on the order of 0.1 eV.

The average deintercalation potential E was calculated as $E = -\Delta H/e$, where ΔH is the enthalpy for the intercalation reaction (in eV) and e is the transferred charge (1 electron). The ΔH is defined as

$$\Delta H = [H(\text{A}_x\text{FePO}_4\text{F}) - H(\text{A}_y\text{FePO}_4\text{F}) - (x - y)H(\text{A})] / (x - y) \quad (1)$$

where $H(\text{A}_x\text{FePO}_4\text{F})$ and $H(\text{A}_y\text{FePO}_4\text{F})$ are the total energies of two compared phases, and $H(\text{A})$ is the energy per alkali atom (Li or Na) in the metallic state with a bcc lattice.

The antisite formation energy is calculated as

$$E_{\text{as}} = E(\text{Na}_2\text{FePO}_4\text{F}, \text{antisite}) - E(\text{Na}_2\text{FePO}_4\text{F}, \text{ideal}) \quad (2)$$

where $E(\text{Na}_2\text{FePO}_4\text{F}, \text{ideal})$ is the total energy of the 144-atom supercell and $E(\text{Na}_2\text{FePO}_4\text{F}, \text{antisite})$ is the total energy of the

same supercell with one antisite defect: exchange of Na and Fe atoms.

RESULTS

Comparative Electrochemistry. The prepared carbon-coated $\text{Na}_2\text{FePO}_4\text{F}$ sample with the single-phase $Pbcn$ structure exhibits nearly 85% of its theoretical capacity in both Li-ion and Na-ion cells (discharge capacity of ~ 105 mAh/g at C/10 rate). Since its electrochemical behavior, C-rate dependence, and capacity retention have already been reported, here we focus only at the first charge process, comparing the samples treated in the Li-ion and Na-ion cells. The normalized $E-x$ dependences collected at C/10 rate in Li-ion and Na-ion cells are presented in Figure 1.

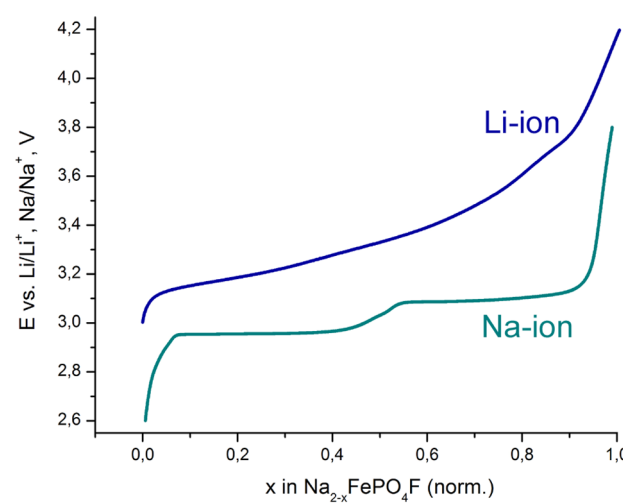


Figure 1. $E-x$ curves for the first charge process of $\text{Na}_2\text{FePO}_4\text{F}$ at C/10 rate in the Li-ion and Na-ion cells.

The first charge of $\text{Na}_2\text{FePO}_4\text{F}$ is expected to be a desodiation process proceeding through the same mechanism in the Li-ion and Na-ion cells, as desodiation is confined to the bulk rather than to the surface and, thus, should not be strongly affected by the nature of the electrolyte. Contrary to these expectations, charging in the Li-ion cell is characterized by a smooth sloping curve typical for a solid solution behavior, while in the Na-ion cell two flat plateaus are present corresponding to two-phase reactions. In the Li-ion cell at the beginning of the charge process, the voltage of the $\text{Fe}^{2+}/\text{Fe}^{3+}$ pair is nearly the same as that for the Na-ion cell, taking into account the relative difference in the potentials of the Li/Li^+ and Na/Na^+ redox pairs. However, the difference between the desodiation potentials grows rapidly with increasing x . This might indicate that $\text{Na}_{2-x}\text{FePO}_4\text{F}$ is supposedly undergoing different electrochemical desodiation processes in the cells differing only by the electrolyte compositions and counter-electrodes, at the same charge rate and temperature. To get additional electrochemical data on this difference in behavior of $\text{Na}_2\text{FePO}_4\text{F}$ in the Li-ion and Na-ion cells, we studied the first desodiation process with a potential intermittent titration technique (PITT) (Figure S1 of the Supporting Information).

As for the galvanostatic charge experiment, the results for the two electrochemical systems differ dramatically. The shape of both $E-t$ and $i-t$ curves obtained via PITT is more typical for the solid solution behavior in the case of Li-ion cells, especially above 50% SOC ($E > 3.3$ V vs. Li/Li^+) (Figure S1a). In

contrast, two distinct two-phase processes at ~ 2.95 and 3.05 V vs Na/Na⁺ are observed in the Na-ion cell (Figure S1,b).³⁶ For the treatment of the raw PITT data we used approximations previously applied for the study of phase transformations behavior in olivine-type cathode materials of different compositions.^{37,38} The estimated amount of charge associated with the contribution of the single-phase (or solid solution) mechanism—*f*—to overall deintercalation process is plotted in Figure S1,c. The *f*-value varies between ~ 0.2 and 0.3 in the case of the Na-ion electrolyte, indicating a two-phase character of the process. For the Li-ion system, the *f*-value increases from ~ 0.4 to 0.8 during the desodiation process, suggesting a change in the deintercalation mechanism, which becomes predominantly a single-phase process at high SOC.

The average Fe oxidation state in the samples half-charged in the Na-ion and Li-ion cells has been confirmed by ⁵⁷Fe Mössbauer spectroscopy (Figure S2 and Table S1). In both samples, the room-temperature spectra consist of two broadened and asymmetric quadrupole doublets with the isomer shifts typical for Fe³⁺ and Fe²⁺ in the octahedral environment.³⁹ The ratio between the areas of the Fe³⁺ and Fe²⁺ doublets is close to 1:1 in both samples. The noticeable broadening of the doublets can tentatively be ascribed to incomplete Na/vacancy and Na/Li ordering causing variations in the second coordination sphere of the Fe cations (Tables S4, S5).

Structural Characterization. In order to clarify the difference between the electrochemical charging mechanisms in the Li-ion and Na-ion cells, we investigated the crystal structures of the half-charged materials with synchrotron X-ray powder diffraction. The sample desodiated in the Na-ion cell shows a monoclinic distortion similar to that reported by Ellis et al.¹⁶ The structure model of this monoclinic phase has been built in the space group *P2*₁/*b* (monoclinic angle α , *P2*₁/*c* in a standard setting), as it is a subgroup of *Pbcn*, the space group of parent Na₂FePO₄F. With this symmetry lowering every position in *Pbcn* (except F1 and F2) splits into two symmetrically inequivalent positions. The refinement of this monoclinic structure has been performed within a rigid body approximation where the geometry of the PO₄ groups was fixed to a perfect tetrahedron with the P–O interatomic distance of 1.544 Å. All atomic positions were refined with a common atomic displacement parameter. The occupancy factors of the A1₁, A1₂ positions (originating from the position A1 in the *Pbcn* structure) and the A2₁, A2₂ positions (originating from the position A2 in the *Pbcn* structure) were included into the refinement. The A1₁ and A2₂ positions are fully occupied, and the A1₂ position contains only a minor fraction of the Na vacancies (<10%) (Figure 2). Almost all Na vacancies are located in the A2₁ position, which is thus the only electrochemically active site at 50% SOC. The refined total sodium content corresponds to the Na/(Fe + P) = 0.775 atomic ratio, in excellent agreement with the ratio of 0.77 determined with EDX analysis (Table S2). The ordering of the Na atoms and vacancies is coupled to the Fe²⁺/Fe³⁺ charge ordering, as indicated by a substantial difference in the average Fe–(O,F) interatomic distances for the positions Fe1 and Fe2 (2.16 and 2.01 Å, respectively). Indeed, the bond valence sum (BVS) method reveals the formal valences of +1.86(3) for the Fe1 position and +2.78(5) for the position Fe2.

A similar refinement strategy has been applied to the sample half-charged in the Li-ion cell. Here, the main phase preserves the *Pbcn* space symmetry, eliminating the possibility of charge

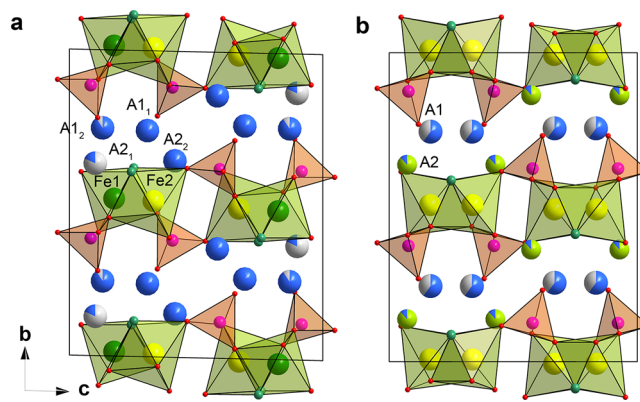


Figure 2. Crystal structures of the half-charged materials Na_{1.55}FePO₄F (a) and Li_{0.88}Na_{0.73}FePO₄F (b). The Fe atoms are shown as dark green/yellow spheres, P atoms, as purple spheres, and O and F atoms, as small red and green spheres, respectively. The A positions demonstrate their actual occupancy with Na (blue), Li (light green), and vacancy (gray); the occupancy factor is proportional to the size of the sectors.

ordering, as there is a single crystallographic Fe position in this structure. The average electron density in the A1 and A2 positions was estimated by populating them with the sodium atoms and refining the occupancy factors. The values of 6.7e⁻ and 3.3e⁻ were obtained for the A1 and A2 position, respectively. However, due to a possible mixing of three entities with different scattering factors (Na, Li, and vacancy) in these crystallographic positions, their atomic populations cannot be assigned uniquely. Interatomic distances provide clear and unambiguous indication on the location of the Li atoms. The average A2–(O,F) distance of 2.16 Å is noticeably smaller than that for the A1 position (2.61 Å) and more suitable for Li⁺ ($r = 0.59$ Å, coordination number CN = 6) rather than for Na⁺ ($r = 0.99$ Å, CN = 6). The Na atoms, being placed in the A2 position, acquire BVS = 2.01, far from their nominal valence, whereas Li demonstrates a more reasonable BVS of 0.79. Thus, the A2 position should be fully occupied by $\sim 0.9\text{Li} + 0.1\text{Na}$, whereas all cation vacancies are located in the position A1, which has been previously considered electrochemically inactive. The refined composition of this phase is Li_{0.88}Na_{0.73}FePO₄F, which also agrees qualitatively with Na/(Fe + P) = 0.5 measured by EDX analysis (Table S2). The discrepancy should be attributed to the admixture of the Na_{1.5}FePO₄F phase in this sample.

The crystallographic parameters of the refined half-charged structures are given in Table S3 of the Supporting Information. The atomic coordinates, occupancy factors, and main interatomic distances are provided in Tables S4, S5 for Na_{1.55}FePO₄F and in Tables S6, S7 for Li_{0.88}Na_{0.73}FePO₄F. The experimental, calculated, and difference diffraction profiles after the Rietveld refinement are shown in Figure S3. The crystal structures are shown in Figure 2. The refinement of the Na_{1.55}FePO₄F and Li_{0.88}Na_{0.73}FePO₄F structures strongly suggests that fast chemical Li-for-Na exchange proceeds simultaneously with the electrochemical extraction of Na⁺. In order to confirm this conjecture, we have performed a chemical Li-for-Na exchange in Na₂FePO₄F immersed in an excess of the Li-ion containing electrolyte. The remaining Na content after 10, 48, and 168 h of the chemical exchange was determined by EDX analysis (Table S2). This experiment demonstrates progressive decrease in the Na content with increasing chemical

exchange time, up to the $\text{Li}_{1.58}\text{Na}_{0.42}\text{FePO}_4\text{F}$ composition. The Na content in the $\text{Na}_2\text{FePO}_4\text{F}$ sample, fully charged in the Li-ion cell, also supports the parallel chemical exchange, as only $\sim 0.2\text{--}0.3$ out of 2 Na atoms (as determined with EDX (Table S2) and the Rietveld refinement (Table S3)) remains in the structure at this state of charge, whereas the charge passed corresponds to removal of 1 Na per formula unit. Such deep exchange could not be performed even after soaking the cathode material in a 30-fold excess of electrolyte during 1 week. Concurring electrochemical extraction of Na^+ and chemical Li-for-Na exchange is additionally evident from the EDX analysis of residual Na content in the half-charged $(\text{Na},\text{Li})_{1.5}\text{FePO}_4\text{F}$ samples obtained at different temperatures. Lowering the temperature down to -10°C suppresses the chemical exchange process, providing the $\text{Na}/(\text{Fe} + \text{P}) = 0.76(5)$ ratio, whereas increasing the temperature to 75°C facilitates faster chemical exchange, decreasing this ratio to $0.32(5)$ at the same 50% SOC (Table S2). Increasing the current rate up to 1C did not lead to a complete suppression of the Na/Li exchange, as it was observed for the low-temperature charging. The difference in the atomic ratios of $((\text{Na}/(\text{Fe} + \text{P}))_{\text{expected}} - (\text{Na}/(\text{Fe} + \text{P}))_{\text{observed}})$ decreases only by 30% after a 20-fold increase of the charge rate from C/20 to 1C.

An intriguing question remains on the desodiation behavior of the A1 and A2 positions at the second half of the charge curve, up to the AFePO_4F composition. Thus, the crystal structure refinement has been performed for the cathodes fully charged in the Na-ion and Li-ion cells. For the material charged in the Na-ion cell, the $Pbcn$ structure is restored, where the A2 position is vacant and the A1 position is fully occupied, corresponding to the NaFePO_4F composition. These results are in agreement with the previous reports, where NaFePO_4F was obtained by a chemical oxidation.^{14,15} The sample charged in the Li-ion cell adopts a similar structure. Difference Fourier maps do not reveal noticeable scattering density in the A2 position. The refinement of the occupancy factor for the position A1 (being populated by the Na atoms) resulted in the electron density corresponding to 4.7e^- that is equal to $0.28\text{Na} + 0.72\text{Li}$ ($\text{Li}_{0.72}\text{Na}_{0.28}\text{FePO}_4\text{F}$ composition). In both structures the average Fe–(O,F) distances are shorter than those in the half-charged materials (2.00 \AA vs 2.08 \AA in full-charged and half-charged Na-ion cells and 1.95 \AA vs 2.02 \AA in full-charged and half-charged Li-ion cells, respectively), indicating further oxidation of iron to Fe^{3+} .

The crystallographic parameters of the refined fully charged structures are given in Table S3. The atomic coordinates, occupancy factors, and main interatomic distances are provided in Tables S8, S9 for NaFePO_4F and in Tables S10, S11 for $\text{Li}_{0.72}\text{Na}_{0.28}\text{FePO}_4\text{F}$. The experimental, calculated, and difference diffraction profiles after the Rietveld refinement are shown in Figure S4. The crystal structures are shown in Figure S5.

To grasp more insight into the behavior of $\text{Na}_2\text{FePO}_4\text{F}$ in the Li-ion half-cell an *operando* SXPD study of the first two charge/discharge cycles was conducted (Figure 3). The phase composition of the electrode and its evolution clearly reflect that the system is driven by a competition of electrochemical alkali ion (de)intercalation and chemical Na/Li exchange. An adequate Rietveld fit requires at least four phases: $\text{Na}_2\text{FePO}_4\text{F}$, charge-ordered $\text{Na}_{1.5}\text{FePO}_4\text{F}$, Na-rich solid solution $(\text{Na},\text{Li})_{2-x}\text{FePO}_4\text{F}$ (with larger unit cell parameters), and Li-rich solid solution $(\text{Li},\text{Na})_{2-x}\text{FePO}_4\text{F}$ (with smaller unit cell parameters). The fractions of the first three phases change concomitantly with the SOC, indicating their involvement in

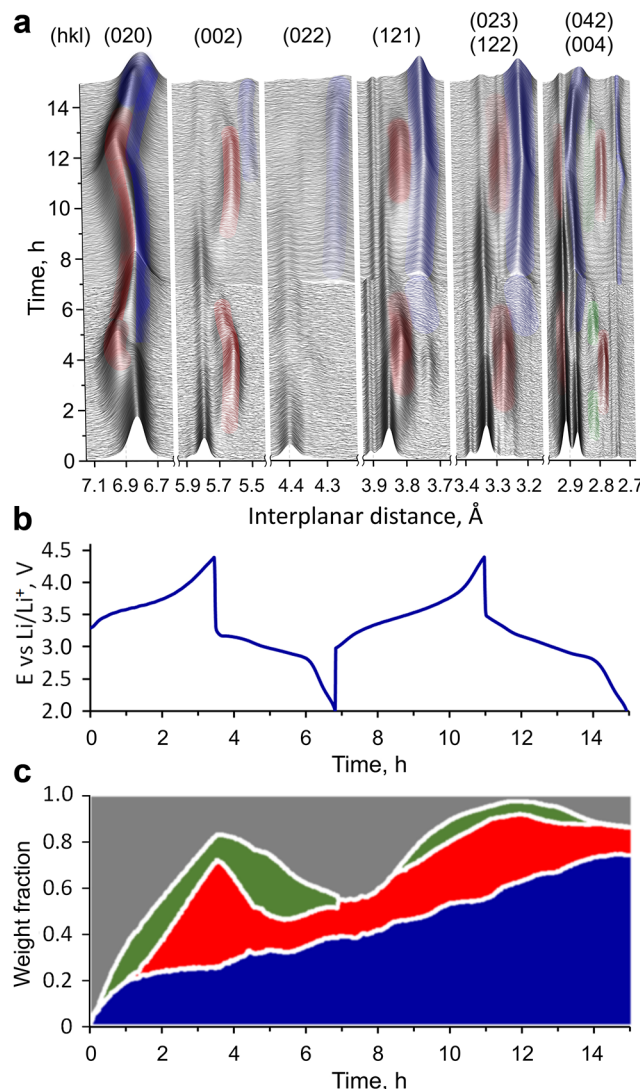


Figure 3. *Operando* SXPD patterns obtained during two charge/discharge cycles in a Li-ion half-cell (a) and corresponding galvanostatic curve (b). Intensity scale is logarithmic. Reflections are marked with colors according to their assignment to the constituting phases: $\text{Na}_2\text{FePO}_4\text{F}$ (gray), $\text{Na}_{1.5}\text{FePO}_4\text{F}$ (green), Na-rich solid solution $(\text{Na},\text{Li})_{2-x}\text{FePO}_4\text{F}$ (red), Li-rich solid solution $(\text{Li},\text{Na})_{2-x}\text{FePO}_4\text{F}$ (blue). The diagram from the batch Rietveld refinement demonstrating the evolution of the phase fractions (c) (color coding is the same as above).

the “two-phase” regime. The content of the fourth Li-rich solid solution $(\text{Li},\text{Na})_{2-x}\text{FePO}_4\text{F}$ phase steadily increases because of progressive chemical exchange. Note that the unit cell parameters of this Li-rich solid solution vary together with SOC, demonstrating that this phase participates in the electrochemical (de)intercalation through a solid solution mechanism. After second discharge this phase becomes dominant in the electrode.

The behavior of the Na-ion system is significantly less complicated. *Operando* XRPD patterns during first charge and their Rietveld refinement show a growing fraction of $\text{Na}_{1.5}\text{FePO}_4\text{F}$ at the expense of $\text{Na}_2\text{FePO}_4\text{F}$ until 50% SOC and NaFePO_4F at the expense of $\text{Na}_{1.5}\text{FePO}_4\text{F}$ until 100% SOC, confirming two subsequent two-phase processes (Figure S6).

The crystal structure analysis of the materials at different SOC was further corroborated by DFT calculations, which address the relative energetics of the A₁ and A₂ positions, intercalation potentials, phase stability, antisite defects, and alkali cation diffusion.

Lattice Constants. The comparison of experimental and theoretical lattice constants is provided in Table S12. For Na compounds GGA PBE overestimates lattice constants by <1%. For Li compounds the GGA PBE overestimates *a* and *c* constants by <2.5%, while the *b* constant, which is highly sensitive to composition, is underestimated by 2% due to the mismatch of cation arrangement between theory and experiment. For the charged in Li-ion cell cathode the LDA predicts *a* and *c* constants in nearly exact agreement with the experimentally measured values.

Deintercalation Potential. The calculated average deintercalation potentials and corresponding volume changes are collected in Table 1. The lower deintercalation potential for the

Table 1. Calculated Average Deintercalation Potential *E* (in V) and Volume Change (%) for Cation Removal from A1 and A2 Positions in Comparison to the Experimental Values^a

couple (X = FePO ₄ F)	<i>E</i>	ΔV	<i>E</i> _{exp}	ΔV _{exp}
Na ₂ X/Na _{1.5} X			2.95	-1.6
A1 = Na _{0.5} □ _{0.5} , A2 = Na	3.08	0.7		
A1 = Na, A2 = Na _{0.5} □ _{0.5}	2.99	-1.6		
Na ₂ X/NaX			3.05	-2.9
A1 = □, A2 = Na	3.24	5.4		
A1 = Na, A2 = □	3.03	-3.7		
NaLiX/(Na _{0.5} LiX, NaLi _{0.5} X)			3.10–4.20	
A1 = Na _{0.5} □ _{0.5} , A2 = Li	2.98	0.8		
A1 = Na, A2 = Li _{0.5} □ _{0.5}	3.12	1.2		
LiNaNX/(NaX, LiX _x)				
A1 = □, A2 = Na	3.33	12.7		
A1 = Li, A2 = □	3.17	-6.2		
NaLiX/(LiX, NaX)				
A1 = □, A2 = Li	3.15	8.3		
A1 = Na, A2 = □	3.18	2.5		

^aThe symbol □ stands for cation vacancy.

complete cation removal from the position A2 (3.03 V) in Na₂FePO₄F (Na₂X/NaX in Table 1) indicates that this position is electrochemically more active than the position A1 (3.24 V), in agreement with the experiment. However, after replacement of Na with Li at A2 in the half-charged material the average potential for A1 (see NaLiX/Na_{0.5}LiX in Table 1) reduces dramatically to 2.98 V. Therefore, the Li for Na substitution at the position A2 activates the A1 position. Interestingly, the removal of Na from the position A1 in Na₂FePO₄F increases the unit cell volume by 5.4%, while in the case of Na removal from the position A2 the volume is reduced by 3.7%. The experimental ΔV values definitely support the second scenario.

To check whether vibrational entropy could affect the relative stability of A1 and A2 sites, we have calculated free energies in harmonic approximation. The dependence of deintercalation potentials determined from free energies is shown in Figure S7 for Na removal from A1 and A2 sites. The figure clearly shows that the relative stability of sites is nearly temperature independent. For both sites the deintercalation potential slowly increases with temperature (by ~0.05 V higher at room temperature).

Phase Stability. The DFT-predicted structure of Na_{1.5}FePO₄F with lowest energy coincides with that shown in Figure 2a, where A₁₂ sites are fully occupied and the A₂₁ sites are empty. In the low-energy structure of Na_{0.5}LiFePO₄F the A₂ positions are substituted with Li, the A₁₂ position is occupied with Na, and the A₁₁ position is empty. The lowest energy structure of Li_{0.75}Na_{0.25}FePO₄F with empty A₂ contains Na in A₁₂ and A₁₁.

To check whether the formation of stable phases is possible at intermediate vacancy concentrations, we have evaluated the phase stabilities for model NaNa_{1-x}FePO₄F (Na extracted only from A₂) and Na_{1-x}LiFePO₄F (Li stays in A₂, Na extracted from A₁) systems. The formation energies, calculated with the cluster expansion method are shown in Figure 4. For both

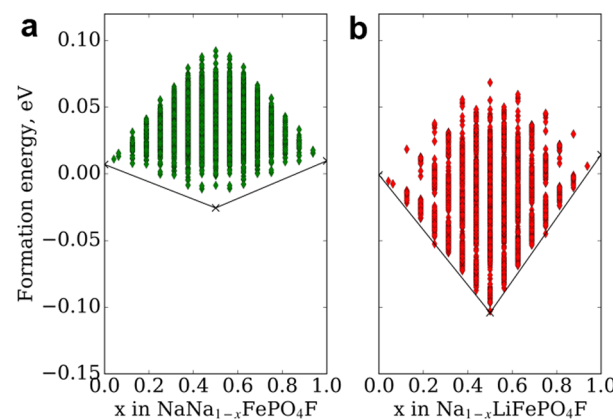


Figure 4. Formation energies calculated using the cluster expansion method (DFT+U based) for two systems, modeling charging in the (a) Na-ion cell and (b) Li-ion cell. All possible configurations for the 144-atom supercell are included. Crosses mark stable phases at *x* = 0, 0.5, and 1.

systems only one additional ground state is observed at *x* = 0.5. This is consistent with the two-phase charging mechanism found in the Na-ion cell. In contrast, for the Li-ion cell the proximity of structures with intermediate concentrations to the convex hull in Figure 4,b suggests that the Na_{1-x}LiFePO₄F system, in agreement with experiment, is close to solid-solution-like behavior (due to entropic factors). More important is the difference in convex hull slopes for NaNa_{1-x}FePO₄F and Na_{1-x}LiFePO₄F systems. In the first case, the change of formation energies with concentration is gentle, implying a voltage plateau during charging. In the second case much steeper change in formation energies with concentration would be responsible for an observed voltage increase upon Na extraction.

The existence of a ground state at *x* = 0.5 confirms the coupled Na-vacancy ordering and Fe²⁺/Fe³⁺ charge ordering both in Na_{1-x}LiFePO₄F and in NaNa_{1-x}FePO₄F system. However, the magnitude of that coupling is lower in the case of Na_{0.5}LiFePO₄F, which is manifested in higher density of structures near the convex hull in consistency with longer A1–Fe separation compared to A2–Fe separation. Presumably, the solid solution behavior observed during charging in the Li-ion cell stems from the much richer configurational space, which is not taken into account in our model system. In particular, as was mentioned in the previous section, the real system is additionally complicated by concurrent Li for Na exchange during Na extraction and the subsequent transition of Li from

the A2 to the A1 position. The detailed computational study of this process is beyond the scope of the current work.

Diffusion of Na and Li. To understand the mechanism of fast Li for Na exchange during charging in the Li-ion cell, we have calculated activation energies of Na and Li diffusion in pristine and charged compounds using the DFT–NEB method. Simple geometrical analysis shows that in the structure provided in Figure 2 only A1–A1 and A1–A2 diffusion paths should be energetically efficient, whereas the A2–A2 path involves very close A–O, A–F, A–A, or A–Fe approaches during migration. Indeed, it was shown by Tripathi et al. using DFT–NEB calculations that A2–A2 paths in $\text{Na}_2\text{FePO}_4\text{F}$ are irrelevant and diffusion is governed only by A1–A1 and A1–A2 jumps along the *a* and *c* directions, respectively.¹⁸ Here, in addition to the Na migration in $\text{Na}_2\text{FePO}_4\text{F}$, we calculated Na migration in NaFePO_4F , as well as Na and Li migration in $\text{NaLiFePO}_4\text{F}$. The values of activation energies for diffusion are collected in Table 2. Two and three nonequivalent relevant

Table 2. DFT+U Calculated Activation Energies (eV) for Na and Li Migration in Several Structures ($X = \text{FePO}_4\text{F}$) along *a* (for limiting A1–A1 transition) and along *c* (for Limiting A1–A2 Transition)^a

path	Na_2X (Na)	$\text{Na}\square X$ (Na)	NaLiX (Na)	NaLiX (Li)
along <i>a</i> A1→A1	0.3	0.25	0.7	0.15
along <i>c</i> A1→A2	0.4	0.6	0.4	0.4

^aThe symbol \square stands for cation vacancy.

paths for A1–A1 and A1–A2 transitions, respectively, are possible. Here we provide the values that limit diffusion along corresponding crystallographic directions. In $\text{Na}_2\text{FePO}_4\text{F}$ the diffusion has two-dimensional character with relatively low activation barriers of 0.3 and 0.4 eV along the *a* and *c* directions, respectively.

Upon desodiation the diffusion of Na becomes faster along *a* and slows down along *c*. The activation barrier along *a* decreases due to the increase of the *b* lattice constant. The lower diffusion activation energies for Li can explain the experimentally observed fast Na by Li exchange.

Antisite Defects. It is known that antisite defects have detrimental influence on ion diffusion pathways in cathode materials. This is especially pronounced in the cases with one-dimensional diffusivity, such as olivine LiFePO_4 with an antisite formation energy of 0.45 eV.⁴⁰ The DFT+U calculated antisite formation energies for $\text{Na}_2\text{FePO}_4\text{F}$ are provided in Table 3. The exchange of closest Na and Fe cations results in the lowest formation energies of 0.52 and 0.47 eV for Na1 and Na2 positions, respectively. While both materials have comparable antisite formation energy, the two-dimensional character of diffusion in $\text{Na}_2\text{FePO}_4\text{F}$ suggests that the presence of antisite

defects should be not as detrimental in $\text{Na}_2\text{FePO}_4\text{F}$ as in LiFePO_4 .

DISCUSSION

Charging Mechanism. According to the analysis of the crystal structures at different SOCs in the Na-ion and Li-ion cells, $\text{Na}_2\text{FePO}_4\text{F}$ demonstrates a unique case of switching the electrochemically active alkali cation position depending on the nature of the alkali metal. In the Na-ion cell the desodiation occurs mostly in a “two-phase” regime, where the intermediate $\text{Na}_{1.5}\text{FePO}_4\text{F}$ phase is formed at near 50% SOC. This phase has lower monoclinic symmetry and gets extra energy gain and stability from a coupled Na-vacancy ordering and $\text{Fe}^{2+}/\text{Fe}^{3+}$ charge ordering. In the monoclinic $P2_1/b$ structure the A2 position of the $Pbcn$ structure splits into one nearly vacant position A2₁ and one fully occupied position A2₂. These positions alternate, forming a zigzag chain along the *a* axis. The $\text{Fe}^{2+}/\text{Fe}^{3+}$ charge ordering manifests itself as two crystallographically distinct Fe positions with noticeably different Fe–(O,F) distances (Figure 2,a, Table S6). Further desodiation occurs through deintercalation of the remaining Na from the position A2 until the $Pbcn$ symmetry is restored in the NaFePO_4F phase (Figure S5,a), in which the charge ordering is suppressed because all Fe cations acquire the oxidation state +3.

The desodiation behavior of $\text{Na}_2\text{FePO}_4\text{F}$ in the Li-ion cell is drastically different. A typical “two-phase” galvanostatic charge curve with two well-defined plateaus changes to a sloping curve characteristic of a “solid solution” mechanism. Up to 50% SOC the Na deintercalation competes with simultaneous Li-for-Na chemical exchange, which targets exclusively the position A2, where 88% of Na is replaced by Li (Figure 2,b). This replacement deactivates the position A2, rendering the position A1 electrochemically active. Thus, the A2 position stays fully occupied up to 50% SOC, suppressing the $\text{Fe}^{2+}/\text{Fe}^{3+}$ charge ordering and a formation of intermediate monoclinic phase. Surprisingly, there is a pronounced A1–A2 intersite exchange of the alkali cations above 50% SOC, as in the fully charged $\text{Li}_{0.72}\text{Na}_{0.28}\text{FePO}_4\text{F}$ all alkali cations reside in the A1 position and the A2 position becomes empty (Figure S5,b). Thus, desodiation of $\text{Na}_2\text{FePO}_4\text{F}$ demonstrates that even within the same structural framework and transition metal redox couple, the relative energies of the alkali metal sites can differ substantially depending on the chemical nature of the alkali cations.

Alkali Cation Site Activity. In order to facilitate understanding of the complex deintercalation behavior of $\text{Na}_2\text{FePO}_4\text{F}$ in the Na-ion and Li-ion cells we should discuss the relative preference of the A1 and A2 position for deintercalation. The A1 and A2 positions in the parent $\text{Na}_2\text{FePO}_4\text{F}$ structure have a very similar oxygen/fluorine environment with a “6 + 1” coordination number and close average $\langle \text{A1}-\text{O},\text{F} \rangle$ and $\langle \text{A2}-\text{O},\text{F} \rangle$ distances (2.50 and 2.45 Å, respectively).¹⁵ From the similarity of the first coordination spheres it is difficult to expect any substantial difference in their desodiation potentials. From the larger average distance, the removal of Na from the position A1 should be slightly easier. Nevertheless, the average calculated potential for the position A2 (3.03 V) indicates that it is electrochemically more active than the position A1 (3.24 V). We ascribe this difference to the number of semilabile oxygens in the coordination environment of the alkali cations: there are three undercoordinated oxygens (O2) bonded to the alkali cation at position A1 and only one in the case of A2 (Figure 5). The semilabile oxygen atom of the

Table 3. DFT+U Calculated Na–Fe Antisite Formation Energies (eV) in $\text{Na}_2\text{FePO}_4\text{F}$ for Na1 and Na2 Sites for Different Na–Fe Separations (Å)

no.	Na site	separation	energy
1	Na1	3.23	0.52
2	Na1	3.69	0.60
3	Na2	3.07	0.47
4	Na2	3.27	0.45
5	Na2	3.36	0.62

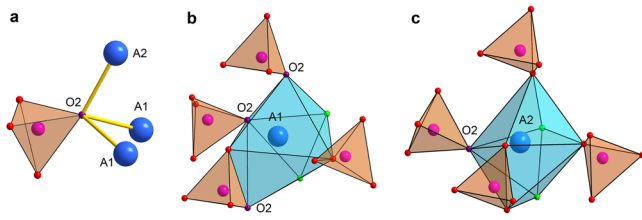


Figure 5. Coordination of the O₂ atoms with the A1 and A2 cations (a). The involvement of the semilabile O₂ atoms in the coordination environment of the A1 (b) and A2 (c) positions. The A atoms are shown as blue spheres, P atoms, as purple spheres, and O and F atoms, as small red and green spheres, respectively. The O₂ atoms are shown as violet spheres.

PO₄ group is linked exclusively to the phosphorus atom and alkali cations and is not directly bonded to a transition metal cation. When the alkali cations are removed upon charging, these semilabile oxygens lose neighboring cations, which causes undercoordination, which is hard to compensate by shortening the P–O distances and/or tighter binding to the remaining alkali cation.¹³ Thus, the alkali cation position surrounded by a larger number of such semilabile oxygens O₂ should be less energetically favorable for desodiation and, hence, less electrochemically active (A1). Removing of the Na atoms from the A1 position in Na₂FePO₄F drastically reduces BVS for the O₂ atoms from 1.98 to 1.55, whereas this reduction is milder if the A2 cations are removed (down to 1.71 only). To make a more rigorous analysis using DFT+U, we have constructed charge density difference (CDD) plots and calculated Bader charges on oxygen atoms, which are provided in Figures 6 and 7, respectively. According to Figure 6,a after

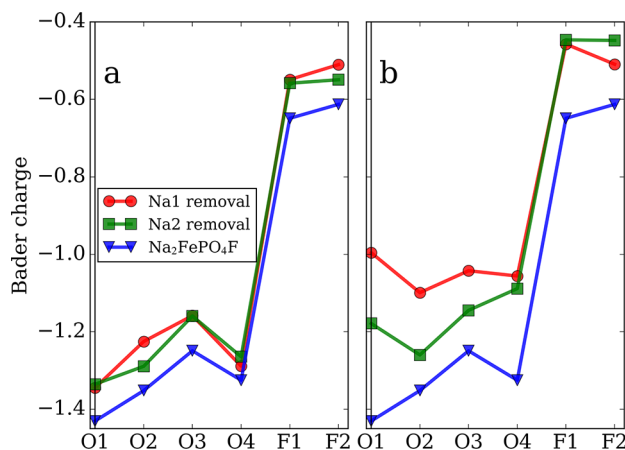


Figure 6. Bader charge on symmetrically nonequivalent oxygen and fluorine atoms in fully optimized Na₂FePO₄F and after Na1 and Na2 removal: (a) without relaxation; (b) after relaxation of all atomic positions and supercell sizes.

the removal of Na from the A1 and A2 positions without relaxation the Bader charges are different only for the O₂ atom and to a less extent for the F₂ atom. The negative charge at O₂ after Na1 removal is 0.07 electron smaller, which confirms the important role of semilabile oxygen atoms and confirms that BVS analysis provides useful physical insights. It can be seen from the CDD plot (Figure 7) that the most pronounced depletion in electron density occurs around the O₂ atom in the case of Na removal from the A1 position. Moreover, the depletions in density around O₁ and O₃ have drop-shaped

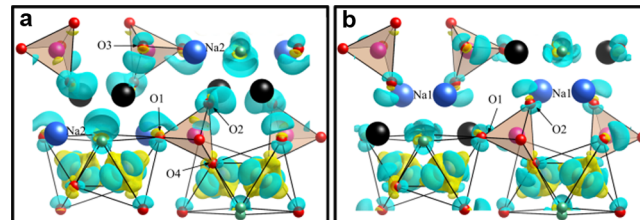
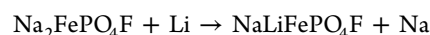


Figure 7. Charge density difference isosurfaces (0.005) calculated as chg(NaFePO₄F) – chg(Na₂FePO₄F) for Na1 removal (a) and Na2 removal (b) without relaxation. The removed Na atoms are shown with black spheres. The negative and positive charge densities are represented with light blue and light yellow shades, respectively. After Na removal the depletion of charge density on oxygen atoms and redistribution of charge density on Fe atoms can be seen. Only the top half of the cell in the same projection as in Figure 2 is shown.

forms with long tails pointing to the P atom, an indication of inductive charge transfer to the O₂ atom. The account of relaxation effects shows considerable restructuring of local coordination and cell sizes after Na removal. In the relaxed fully deintercalated NaFePO₄F structures, the ⟨A1–O,F⟩ average distance is 2.55 Å, while the average ⟨A2–O,F⟩ distance is 2.62 Å. Even more pronounced differences of 10% are manifested in the minimum ($d_{\min}(A2-O2) = 2.16 \text{ \AA}$, $d_{\min}(A1-O2) = 2.39 \text{ \AA}$) and maximum ($d_{\max}(A2-O1) = 3.18 \text{ \AA}$, $d_{\max}(A1-O2) = 2.85 \text{ \AA}$) Na–O distances. It is seen that, after removal of Na1, the O–F polyhedron around Na2 is highly distorted with atypically short bonds with a semilabile O₂ atom, significantly smaller than the sum of the ionic radii ($r(\text{Na}^+, \text{CN} = 7) = 1.12 \text{ \AA}$, $r(\text{O}^{2-}, \text{CN} = 2) = 1.35 \text{ \AA}$). The structural relaxation is accompanied by severe charge redistribution. As it is seen from Figure 6,b, the Bader charge on oxygen atoms is further increased upon relaxation, including O₁ and O₃ atoms, especially after Na1 removal. In both deintercalated cases O₂ is the most negatively charged oxygen position, similar to that discovered in our previous work.³⁰ In contrast to the oxygen atoms, the F₂ atom is more negatively charged after Na1 removal (Figure 6b), suggesting Na2 stabilization. Such behavior contradicts the observed site activity and highlights the predominant influence of oxygen species on the desodiation sequence.

More pronounced charge redistribution on oxygen atoms upon Na1 removal in comparison to Na2 removal explains the higher potential for Na1 deintercalation. The Na2 removal results in better structural optimization, which maximizes the Coulomb attraction and reduces the volume to 840 Å³ in comparison to 920 Å³ after Na1 removal.¹² One of the main reasons triggering different optimization of the two deintercalated structures is the different number of semilabile oxygen atoms around the Na1 and Na2 cations.

Chemical Na by Li Substitution. The chemical substitution of Li for Na also occurs preferentially at the position A2. The DFT-calculated enthalpy for the reaction

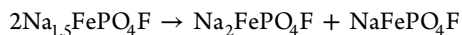


is -0.15 eV for the substitution at the position A2 and -0.08 eV at the position A1. This energy preference of the substitution of larger Na⁺ by smaller Li⁺ might be related to the slightly shorter average ⟨A2–O,F⟩ distance compared to that for the A1 position.

Thus, charging Na₂FePO₄F in the Li-ion cell proceeds in parallel with the chemical exchange of Na for Li at the position

A2. This introduces a dramatic difference in the coordination sphere of the alkali cations: in half-charged $\text{Li}_{0.88}\text{Na}_{0.73}\text{FePO}_4\text{F}$ the position A1 remains 7-fold coordinated and the average $\langle \text{A}1-\text{O},\text{F} \rangle$ interatomic distance increases significantly from 2.50 to 2.61 Å, whereas the coordination number of the A2 position decreases to 5 with the average $\langle \text{A}2-\text{O},\text{F} \rangle$ interatomic distance of only 2.16 Å, which is more suitable for the Li^+ cations rather than for the Na^+ cations. This anionic rearrangement reduces the average deintercalation potential for the A1 position to 2.98 V, rendering it electrochemically active. The Na deintercalation occurs from the position A1, whereas the position A2 remains fully occupied (preferentially by Li).

In contrast, Na extraction from $\text{Na}_2\text{FePO}_4\text{F}$ in the Na-ion cell proceeds from the position A2. Instead of following the solid solution behavior, the desodiation adopts a two-phase mechanism, where the intermediate half-charged $\text{Na}_{1.55}\text{FePO}_4\text{F}$ phase is stabilized by coupled Na-vacancy ordering and $\text{Fe}^{2+}/\text{Fe}^{3+}$ charge ordering, as indicated by a positive DFT-calculated enthalpy of +0.04 eV for the decomposition reaction



Strong coupling between vacancy ordering and charge ordering in $\text{Na}_{1.55}\text{FePO}_4\text{F}$ (partially deintercalated A2 sites) and much weaker coupling in $\text{Li}_{0.88}\text{Na}_{0.73}\text{FePO}_4\text{F}$ (partially deintercalated A1 sites) stems from the weaker interaction between the Fe atoms and alkali cations in the A1 position compared to that in the A2 position. This correlates with the longer A1–Fe (4.01 Å) and shorter A2–Fe (3.33 Å) separations. The CDD for $\text{Na}_{1.5}\text{FePO}_4\text{F}$ is shown in Figure S8, where charge ordering on Fe atoms can be clearly seen. The depletion of electron density at t_{2g} bands and accumulation at e_g^b on Fe1 atoms result in less ionic Fe–O bonding after Na removal.

After 50% SOC, the desodiation proceeds from the A2 positions in both Li-ion and Na-ion cells. In the Li case it must be accompanied by a migration of the alkali cations from the position A2 to the position A1, as in fully charged $\text{Li}_{0.72}\text{Na}_{0.28}\text{FePO}_4\text{F}$ this position appears to be fully occupied. This further stresses the importance of the bond valence compensation for the semilabile O2 oxygens of the PO_4 groups, which is better delivered by the A1 alkali cations rather than the A2 cations, forming only one bond with these oxygens.

CONCLUSIONS

A comparative study of desodiation of orthorhombic layered $\text{Na}_2\text{FePO}_4\text{F}$ in the Na-ion and Li-ion cells demonstrates the importance of the semilabile oxygen atoms of the PO_4 groups (i.e., the oxygen atoms linked only to the P and alkali cations) for the electrochemical behavior of the crystallographically distinct alkali cations. The alkali cation positions A1 and A2 in $\text{Na}_2\text{FePO}_4\text{F}$ have a virtually identical coordination environment, and the difference in their deintercalation behavior can be ascribed to a different number of bonds to the semilabile oxygen atoms. The alkali cations with larger involvement of semilabile oxygens into the first coordination sphere (position A1 in the $\text{Na}_2\text{FePO}_4\text{F}$ structure) are characterized by higher deintercalation potential, which renders them less active for electrochemical desodiation. The desodiation in the Na-ion cell occurs at the position A2 with short contacts to the Fe atoms causing coupled Na/vacancy ordering and $\text{Fe}^{2+}/\text{Fe}^{3+}$ charge ordering, stabilizing the intermediate monoclinic phase and driving the desodiation reaction mainly through the two-phase

mechanism. Contrarily, desodiation in the Li-ion cell tends to proceed through the solid solution mechanism. Chemical Li-for-Na exchange at the A2 position drastically shortens the A2–O,F interatomic distances and weakens the A1–O,F bonds, activating the A1 position for electrochemical deintercalation and suppressing the charge ordering due to longer A1–Fe contacts. At the end of charge all cation vacancies reside in the A2 positions because the presence of the A1 cations is vitally important to prevent undercoordination of the semilabile oxygens in the fully charged structures. Thus, we identify the interactions with the semilabile oxygen atoms as an important factor that must be taken into account while discussing electrochemical activity of alkali cations in the polyanion structures.

ASSOCIATED CONTENT

S Supporting Information

The Supporting Information is available free of charge on the ACS Publications website at DOI: [10.1021/jacs.7b12644](https://doi.org/10.1021/jacs.7b12644).

Additional information ([PDF](#))

X-ray crystallographic data ([CIF](#))

([CIF](#))

([CIF](#))

([CIF](#))

AUTHOR INFORMATION

Corresponding Author

*E-mail: a.abakumov@skoltech.ru.

ORCID

Alexey V. Sobolev: [0000-0002-8085-5425](#)

Andriy Zhugayevych: [0000-0003-4713-1289](#)

Keith J. Stevenson: [0000-0002-1082-2871](#)

Artem M. Abakumov: [0000-0002-7135-4629](#)

Notes

The authors declare no competing financial interest.

ACKNOWLEDGMENTS

This work was supported by the Russian Science Foundation (Grant No. 17-73-30006), Skolkovo Institute of Science and Technology, and the Lomonosov Moscow State University Program of Development. Dmitry Chernyshov is acknowledged for help with collecting SXPD data.

REFERENCES

- Melot, B. C.; Tarascon, J.-M. *Acc. Chem. Res.* **2013**, *46*, 1226–1238.
- Goodenough, J. B.; Kim, Y. *Chem. Mater.* **2010**, *22*, 587–603.
- Gutierrez, A.; Benedek, N. A.; Manthiram, A. *Chem. Mater.* **2013**, *25*, 4010–4016.
- Masquelier, C.; Padhi, A. K.; Nanjundaswamy, K. S.; Goodenough, J. B. *J. Solid State Chem.* **1998**, *135*, 228–234.
- Manthiram, A.; Goodenough, J. B. *J. Power Sources* **1989**, *26*, 403–408.
- Padhi, K.; Nanjundaswamy, K. S.; Goodenough, J. B. *J. Electrochem. Soc.* **1997**, *144*, 1188–1194.
- Dom Pablo, M. E. A. D.; Rozier, P.; Morcrette, M.; Tarascon, J.-M. *Chem. Mater.* **2007**, *19*, 2411–2422.
- Sirisopanaporn, C.; Masquelier, C.; Bruce, P. G.; Armstrong, A. R.; Dominko, R. *J. Am. Chem. Soc.* **2011**, *133*, 1263–1265.
- Yamada, A.; Iwane, N.; Harada, Y.; Nishimura, S.; Koyama, Y.; Tanaka, I. *Adv. Mater.* **2010**, *22*, 3583–3587.

- (10) Legagneur, V.; An, Y.; Mosbah, A.; Portal, R.; le Gal la Salle, A.; Verbaere, A.; Guyomard, D.; Piffard, Y. *Solid State Ionics* **2001**, *139*, 37–46.
- (11) Yakubovich, O. V.; Simonov, M. A.; Belov, N. V. *Dokl. Akad. Nauk SSSR* **1977**, *235*, 93–95.
- (12) Melot, B. C.; Scanlon, D. O.; Reynaud, M.; Rousse, G.; Chotard, J.-N.; Henry, M.; Tarascon, J.-M. *ACS Appl. Mater. Interfaces* **2014**, *6*, 10832–10839.
- (13) Karakulina, O. M.; Khasanova, N. R.; Drozhzhin, O. A.; Tsirlin, A. A.; Hadermann, J.; Antipov, E. V.; Abakumov, A. M. *Chem. Mater.* **2016**, *28*, 7578–7581.
- (14) De la Rochère, M.; Kahn, A.; d'Yvoire, F.; Bretey, E. *Mater. Res. Bull.* **1985**, *20*, 27–34.
- (15) Fedotov, S. S.; Kabanov, A. A.; Kabanova, N. A.; Blatov, V. A.; Zhugayevych, A. Ya.; Abakumov, A. M.; Khasanova, N. R.; Antipov, E. V. *J. Phys. Chem. C* **2017**, *121*, 3194–3202.
- (16) Ellis, B. L.; Makahnouk, W. R. M.; Makimura, Y.; Toghill, K.; Nazar, L. F. *Nat. Mater.* **2007**, *6*, 749–753.
- (17) Ellis, B. L.; Makahnouk, W. R. M.; Rowan-Weetaluktuk, W. N.; Ryan, D. H.; Nazar, L. F. *Chem. Mater.* **2010**, *22*, 1059–1070.
- (18) Tripathi, R.; Wood, S. M.; Islam, M. S.; Nazar, L. F. *Energy Environ. Sci.* **2013**, *6*, 2257–2264.
- (19) Song, W.; Ji, X.; Wu, Zh.; Zhu, Y.; Yao, Y.; Huangfu, K.; Chen, Q.; Banks, C. E. *J. Mater. Chem. A* **2014**, *A2*, 2571–2577.
- (20) Petricek, V.; Dusek, M.; Palatinus, L. Z. *Kristallogr. - Cryst. Mater.* **2014**, *229*, 345–352.
- (21) Rodríguez-Carvajal, J. *Commission on Powder Diffraction (IUCr)* **2001**, *26*, 12–19.
- (22) Roisnel, T.; Rodriguez-Carvajal, J. *Mater. Sci. Forum* **2001**, *378–381*, 118–123.
- (23) Leriche, J. B.; Hamelet, S.; Shu, J.; Morcrette, M.; Masquelier, C.; Ouvrard, G.; Zerrouki, M.; Soudan, P.; Belin, S.; Elkaïm, E.; Baudelet, F. *J. Electrochem. Soc.* **2010**, *157*, A606–A610.
- (24) Drozhzhin, O. A.; Tereshchenko, I. V.; Emerich, H.; Antipov, E. V.; Abakumov, A. M.; Chernyshov, D. *J. Synchrotron Radiat.* **2018**, *25*, 468–472.
- (25) Matsnev, M. E.; Rusakov, V. S. *AIP Conf. Proc.* **2012**, *1489*, 178. Matsnev, M. E.; Rusakov, V. S. *AIP Conf. Proc.* **2014**, *1622*, 40.
- (26) Kresse, G.; Furthmüller, J. *Comput. Mater. Sci.* **1996**, *6*, 15–50.
- (27) Hohenberg, P.; Kohn, W. *Phys. Rev.* **1964**, *136* (3B), B864–B871.
- (28) Kohn, W.; Sham, L. *J. Phys. Rev.* **1965**, *140* (4A), A1133–A1138.
- (29) Perdew, J.; Burke, K.; Ernzerhof, M. *Phys. Rev. Lett.* **1996**, *77* (18), 3865–3868.
- (30) Blöchl, P. E. *Phys. Rev. B: Condens. Matter Mater. Phys.* **1994**, *50* (24), 17953.
- (31) Dudarev, S. L.; Botton, G. A.; Savrasov, S. Y.; Humphreys, C. J.; Sutton, A. P. *Phys. Rev. B: Condens. Matter Mater. Phys.* **1998**, *57* (3), 1505–1509.
- (32) Jain, A.; Hautier, G.; Moore, C. J.; Ping Ong, Sh.; Fischer, C. C.; Mueller, T.; Persson, K. A.; Ceder, G. A. *Comput. Mater. Sci.* **2011**, *50* (8), 2295–2310.
- (33) Meredig, B.; Thompson, A.; Hansen, H. A.; Wolverton, C.; Van De Walle, A. *Phys. Rev. B: Condens. Matter Mater. Phys.* **2010**, *82*, 2–6.
- (34) Togo, A.; Tanaka, I. *Scr. Mater.* **2015**, *108*, 1–5.
- (35) Van de Walle, A.; Asta, M.; Ceder, G. *CALPHAD: Comput. Coupling Phase Diagrams Thermochem.* **2002**, *26*, 539–553.
- (36) Levi, M. D.; Aurbach, D. *J. Solid State Electrochem.* **2007**, *11*, 1031–1042.
- (37) Ravnsbæk, D. B.; Xiang, K.; Xing, W.; Borkiewicz, O. J.; Wiaderek, K. M.; Gonet, P.; Chapman, K. W.; Chupas, P. J.; Chiang, Y.-M. *Nano Lett.* **2014**, *14*, 1484–1491.
- (38) Drozhzhin, O. A.; Sumanov, V. D.; Karakulina, O. M.; Abakumov, A. M.; Hadermann, J.; Baranov, A. N.; Stevenson, K. J.; Antipov, E. V. *Electrochim. Acta* **2016**, *191*, 149–157.
- (39) Menil, F. *J. Phys. Chem. Solids* **1985**, *46*, 763–789.
- (40) Chung, S. Y.; Choi, S. Y.; Lee, S.; Ikuhara, Y. *Phys. Rev. Lett.* **2012**, *108* (19), 1–5.

Supporting information for

The role of semi-labile oxygen atoms for intercalation chemistry of the metal-ion battery polyanion cathodes

Ivan V. Tereshchenko, Dmitry A. Aksyonov, Oleg A. Drozhzhin, Igor A. Presniakov, Alexey V. Sobolev, Andriy Zhugayevych, Daniil Striukov, Keith J. Stevenson, Evgeny Antipov, Artem M. Abakumov

Corresponding Author e-mail: a.abakumov@skoltech.ru

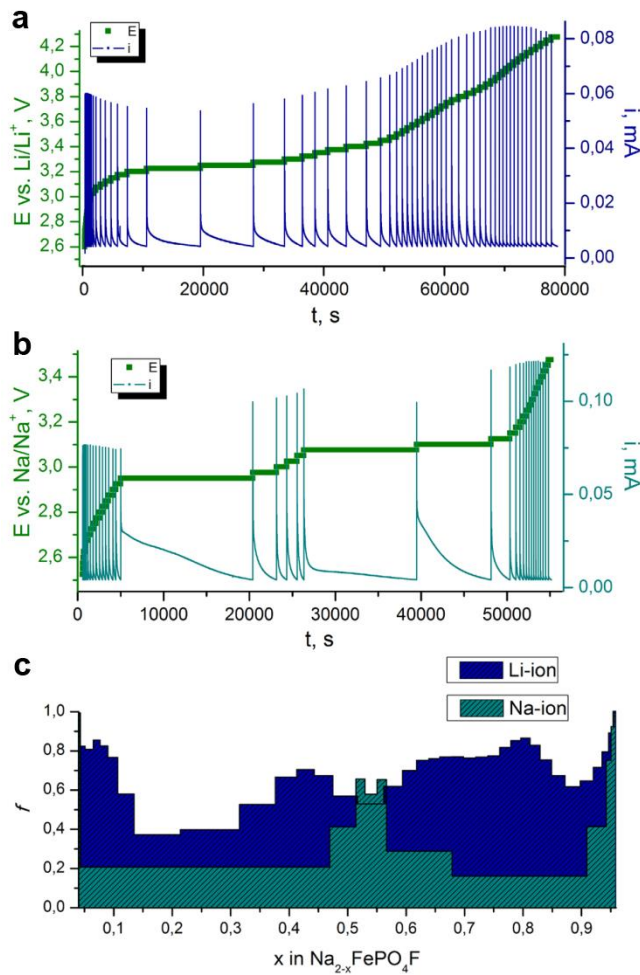


Figure S1. E - t and i - t curves obtained via PITT experiments (25 mV step, C/50 cutoff) for Na₂FePO₄F electrodes in Li-ion (a) and Na-ion (b) cells, and corresponding amount of charge, associated with the contribution of the single-phase mechanism f (c).

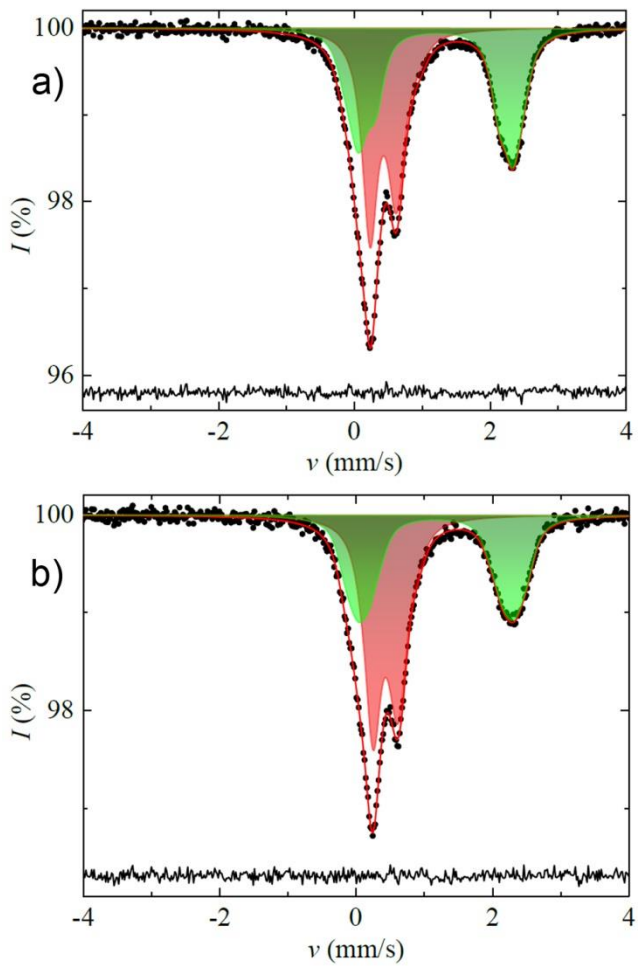


Figure S2. ^{57}Fe Mössbauer spectra of the $\text{Na}_2\text{FePO}_4\text{F}$ electrodes half-charged in the Na-ion (a) and Li-ion (b) cells. The Fe^{3+} and Fe^{2+} doublets are marked with red and green, respectively.

Table S1. Parameters of the ^{57}Fe Mössbauer spectra for the $\text{Na}_2\text{FePO}_4\text{F}$ electrodes half-charged in the Na-ion and Li-ion cells (δ – isomer shift, Δ – quadrupole splitting, W – linewidth, I – relative peak area)

Sample		$\langle \delta_{\text{Fe}} \rangle$, mm/s	$\langle \Delta_{\text{Fe}} \rangle$, mm/s	W , mm/s	I , %
Half-charged in the Na-ion cell	Fe^{3+}	0.434(2)	0.417(4)	0.244(6)*	48.6(3)
	Fe^{2+}	1.202(2)	2.183(4)	0.244(6)*	51.4(3)
Half-charged in the Li-ion cell	Fe^{3+}	0.437(2)	0.395(5)	0.250(7)*	54.7(3)
	Fe^{2+}	1.171(3)	2.201(6)	0.250(7)*	45.3(3)

Table S2. EDX data for the Na₂FePO₄F electrodes at different SOC (C/10 current) and after chemical exchange in Li-ion electrolyte.

Sample	Na/(Fe+P) expected from the charge passed	Na/(Fe+P) from EDX, ± 0.05
Initial	1	1.04
Half-charged in Li-ion cell at -10 °C	0.75	0.76
Half-charged in Li-ion cell at room temperature	0.75	0.50
Half-charged in Li-ion cell at 75 °C	0.75	0.32
Half-charged in Na-ion cell	0.75	0.77
Charged in Li-ion cell	0.5	0.09
Charged in Na-ion cell	0.5	0.67*
Soaked in 30-fold excess of Li-ion electrolyte for 10 h		0.71
Soaked in 30-fold excess of Li-ion electrolyte for 48 h		0.39
Soaked in 30-fold excess of Li-ion electrolyte for 168 h		0.21

*some Na excess with respect to expected value may appear due to incomplete charge of the electrode

Table S3. Crystallographic data for $\text{Na}_2\text{FePO}_4\text{F}$ half-charged in the Na-ion and Li-ion cells. The unit cell parameters and space groups are given in Table S3.

Sample	Half-charged in	Half-charged in	Charged in Na-	Charged in Li-ion
	Na-ion cell	Li-ion cell	ion cell	cell
Formula	$\text{Na}_{1.55}\text{FePO}_4\text{F}$	$\text{Li}_{0.88}\text{Na}_{0.73}\text{FePO}_4\text{F}$	NaFePO_4F	$\text{Li}_{0.72}\text{Na}_{0.28}\text{FePO}_4\text{F}$
Z	8	8	8	8
ρ , g/cm ³	3.266	3.283	3.109	3.139
Radiation	Synchrotron X-ray $\lambda = 0.7121 \text{ \AA}$	Synchrotron X-ray $\lambda = 0.7121 \text{ \AA}$	Synchrotron X-ray $\lambda = 0.7121 \text{ \AA}$	Synchrotron X-ray $\lambda = 0.7121 \text{ \AA}$
2θ range, deg.	2.6 – 41.3	2.7 – 41.2	2.6 – 35.2	2.3 – 41.4
Number of reflections	988	508	358	510
Parameters refined	40	21	16	17
R_F , R_P , R_{wP}	0.040, 0.019, 0.026	0.045, 0.022, 0.030	0.032, 0.030, 0.043	0.058, 0.021, 0.031

Table S4. Fractional atomic coordinates, occupancy factors and atomic displacement parameters for Na₂FePO₄F half-charged in the Na-ion cell.

Atom	Position	Occupancy	x/a	y/b	z/c	U _{iso} , Å ²
A1 ₁	4e	1 Na	0.267(3)	0.2389(8)	0.3079(9)	0.0159(8)
A1 ₂	4e	0.91(1) Na	0.743(4)	0.2448(7)	0.1309(7)	0.0159(8)
A2 ₁	4e	0.18(1) Na	0.150(9)	0.128(4)	0.102(4)	0.0159(8)
A2 ₂	4e	1 Na	0.739(4)	0.1423(8)	0.4164(8)	0.0159(8)
Fe1	4e	1	0.2337(15)	0.0096(3)	0.3316(3)	0.0159(8)
Fe2	4e	1	0.7641(16)	0.0146(3)	0.1765(4)	0.0159(8)
P1	4e	1	0.216(2)	0.3832(4)	0.0839(5)	0.0159(8)
P2	4e	1	0.803(2)	0.3819(4)	0.4064(5)	0.0159(8)
O1	4e	1	0.261(4)	0.4000(7)	0.9536(8)	0.0159(8)
O2	4e	1	0.283(4)	0.2781(7)	0.1115(8)	0.0159(8)
O3	4e	1	0.389(2)	0.452(1)	0.156(1)	0.0159(8)
O4	4e	1	0.932(2)	0.403(1)	0.114(1)	0.0159(8)
O5	4e	1	0.729(3)	0.3818(8)	0.5361(9)	0.0159(8)
O6	4e	1	0.709(3)	0.2876(8)	0.3472(9)	0.0159(8)
O7	4e	1	0.675(2)	0.4684(9)	0.348(1)	0.0159(8)
O8	4e	1	0.097(2)	0.3898(9)	0.394(1)	0.0159(8)
F1	4e	1	0.984(4)	0.1163(13)	0.254(2)	0.0159(8)
F2	4e	1	0.501(4)	0.1032(11)	0.244(2)	0.0159(8)

Table S5. Fractional atomic coordinates, occupancy factors and atomic displacement parameters for Na₂FePO₄F half-charged in the Li-ion cell.

Atom	Position	Occupancy	x/a	y/b	z/c	U _{iso} , Å ²
A1	8d	0.61(1)Na	0.311(3)	0.245(2)	0.333(1)	0.008(1)
A2	8d	0.12(1)Na 0.88(1)Li	0.234(10)	0.137(2)	0.072(3)	0.008(1)
Fe1	8d	1	0.244(2)	0.0070(4)	0.3352(3)	0.008(1)
P1	8d	1	0.234(1)	0.3750(6)	0.0778(6)	0.008(1)
O1	8d	1	0.358(3)	0.3849(6)	0.9519(8)	0.008(1)
O2	8d	1	0.244(3)	0.2686(6)	0.1175(8)	0.008(1)
O3	8d	1	0.393(2)	0.4372(9)	0.1672(9)	0.008(1)
O4	8d	1	0.941(2)	0.4093(9)	0.0745(9)	0.008(1)
F1	4c	1	0	0.085(2)	1/4	0.008(1)
F2	4c	1	1/2	0.088(2)	1/4	0.008(1)

Table S6. Selected interatomic distances for Na₂FePO₄F half-charged in the Na-ion cell.

Bond		Bond	
A1 ₁ -O2	2.34(1)	A2 ₂ -O5	2.63(2)
A1 ₁ -O5	2.50(2)	A2 ₂ -O5	2.73(2)
A1 ₁ -O6	2.44(2)	A2 ₂ -O6	2.20(2)
A1 ₁ -O8	2.47(2)	A2 ₂ -O7	2.57(2)
A1 ₁ -F1	2.33(2)	A2 ₂ -O8	2.36(2)
A1 ₁ -F2	2.70(2)	A2 ₂ -F1	2.29(3)
<i>BVS</i>	0.98(2)	A2 ₂ -F2	2.39(2)
		<i>BVS</i>	1.11(2)
A1 ₂ -O1	2.22(1)	Fe1-O3	2.25(1)
A1 ₂ -O2	2.45(3)	Fe1-O5	2.12(1)
A1 ₂ -O2	2.86(3)	Fe1-O7	2.21(1)
A1 ₂ -O2	2.82(1)	Fe1-O8	2.03(1)
A1 ₂ -O4	2.42(2)	Fe1-F1	2.18(2)
A1 ₂ -O6	2.56(1)	Fe1-F2	2.17(2)
A1 ₂ -F1	2.63(3)	<i>BVS</i>	1.86(3)
A1 ₂ -F2	2.70(2)		
<i>BVS</i>	0.97(2)	Fe2-O1	1.93(1)
		Fe2-O3	2.02(1)
A2 ₁ -O1	2.16(5)	Fe2-O4	1.98(2)
A2 ₁ -O2	2.20(6)	Fe2-O7	2.12(1)
A2 ₁ -O3	2.56(6)	Fe2-F1	2.01(2)
A2 ₁ -O4	2.92(5)	Fe2-F2	1.99(2)
A2 ₁ -F1	1.97(6)	<i>BVS</i>	2.78(5)
A2 ₁ -F2	2.49(5)		
<i>BVS</i>	1.37(10)	P - O	1.544(1)

Table S7. Selected interatomic distances for Na₂FePO₄F half-charged in the Li-ion cell.

Bond		Bond	
A1-O1	2.39(2)	Fe1-O1	2.06(1)
A1-O2	2.32(2)	Fe1-O3	2.01(1)
A1-O2	2.46(2)	Fe1-O3	2.22(1)
A1-O2	2.85(2)	Fe1-O4	1.96(1)
A1-O4	2.81(2)	Fe1-F1	1.89(2)
A1-F1	2.87(3)	Fe1-F2	1.96(2)
A1-F2	2.55(3)	<i>BVS</i>	2.74(4)
<i>BVS</i>	0.79(2)	P – O	1.544(1)
A2-O1	1.93(5)		
A2-O2	1.90(3)		
A2-O4	2.05(4)		
A2-F1	2.42(4)		
A2-F2	2.49(4)		
<i>BVS(Na)</i>	2.01(11)		
<i>BVS(Li)</i>	0.88(3)		

Table S8. Fractional atomic coordinates, occupancy factors and atomic displacement parameters for Na₂FePO₄F fully charged in the Na-ion cell.

Atom	Position	Occupancy	x/a	y/b	z/c	U _{iso} , Å ²
A1	8d	1 Na	0.252(3)	0.2508(6)	0.3425(7)	0.0064(9)
Fe1	8d	1	0.229(1)	0.0198(2)	0.3314(3)	0.0064(9)
P1	8d	1	0.199(1)	0.3865(3)	0.0928(3)	0.0064(9)
O1	8d	1	0.244(3)	0.3884(7)	0.9590(7)	0.0064(9)
O2	8d	1	0.277(3)	0.2882(7)	0.1413(7)	0.0064(9)
O3	8d	1	0.366(2)	0.4642(9)	0.1518(9)	0.0064(9)
O4	8d	1	0.908(2)	0.4081(9)	0.1193(9)	0.0064(9)
F1	4c	1	0	0.102(2)	1/4	0.0064(9)
F2	4c	1	1/2	0.091(2)	1/4	0.0064(9)

Table S9. Fractional atomic coordinates, occupancy factors and atomic displacement parameters for Na₂FePO₄F fully charged in the Li-ion cell.

Atom	Position	Occupancy	x/a	y/b	z/c	U _{iso} , Å ²
A1	8d	0.28(1)Na 0.72(1)Li	0.272(7)	0.254(3)	0.338(2)	0.0024(9)
Fe1	8d	1	0.245(2)	0.0036(6)	0.3366(3)	0.0024(9)
P1	8d	1	0.236(1)	0.3783(3)	0.0769(5)	0.0024(9)
O1	8d	1	0.362(3)	0.3950(6)	0.9511(8)	0.0024(9)
O2	8d	1	0.239(3)	0.2702(6)	0.1061(8)	0.0024(9)
O3	8d	1	0.398(2)	0.433(1)	0.1736(8)	0.0024(9)
O4	8d	1	0.942(2)	0.415(1)	0.0768(8)	0.0024(9)
F1	4c	1	0	0.078(3)	1/4	0.0024(9)
F2	4c	1	1/2	0.074(3)	1/4	0.0024(9)

Table S10. Selected interatomic distances for Na₂FePO₄F fully charged in the Na-ion cell.

Bond		Bond	
A1-O1	2.37(1)	Fe1-O1	1.951(9)
A1-O2	2.36(1)	Fe1-O3	2.03(1)
A1-O2	2.48(2)	Fe1-O3	2.25(1)
A1-O2	2.77(2)	Fe1-O4	1.94(1)
A1-O4	2.36(2)	Fe1-F1	1.90(2)
A1-F1	2.68(2)	Fe1-F2	1.95(1)
A1-F2	2.79(2)	<i>BVS</i>	3.03(4)
<i>BVS</i>	0.90(2)	P – O	1.544(9)

Table S11. Selected interatomic distances for Na₂FePO₄F fully charged in the Li-ion cell.

Bond		Bond	
A1-O1	2.52(4)	Fe1-O1	1.97(1)
A1-O2	2.58(2)	Fe1-O3	1.99(1)
A1-O2	2.98(2)	Fe1-O3	2.17(1)
A1-O2	2.63(4)	Fe1-O4	1.85(1)
A1-O2	2.51(4)	Fe1-F1	1.87(3)
A1-O3	2.99(5)	Fe1-F2	1.87(2)
A1-O4	2.66(5)	BVS	3.46(7)
A1-F1	2.97(6)	P – O	1.54(1)
A1-F2	2.93(6)		
BVS(Na)	0.68(3)		
BVS(Li)	0.62(1)		

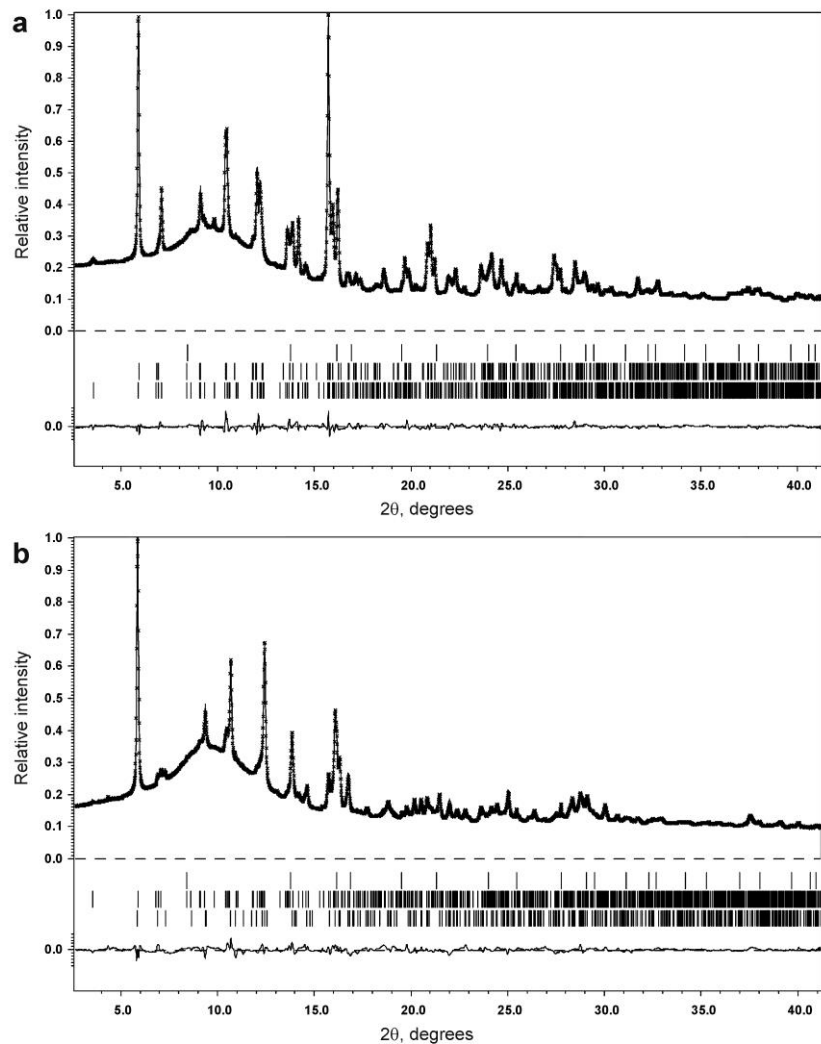


Figure S3. Experimental, calculated and difference SXPD profiles after the Rietveld refinement of $\text{Na}_{1.55}\text{FePO}_4\text{F}$ (a) and $\text{Li}_{0.88}\text{Na}_{0.73}\text{FePO}_4\text{F}$ (b). The bars mark the reflection positions (a: $\text{Na}_{1.55}\text{FePO}_4\text{F}$ (bottom row), $\text{Na}_2\text{FePO}_4\text{F}$ (11 wt.%, middle row) and Fe_3O_4 (1.9 wt.%, top row); b: $\text{Li}_{0.88}\text{Na}_{0.73}\text{FePO}_4\text{F}$ (bottom row), $\text{Na}_{1.5}\text{FePO}_4\text{F}$ (30.6 wt.%, middle row), Fe_3O_4 (2.0 wt.%, top row)).

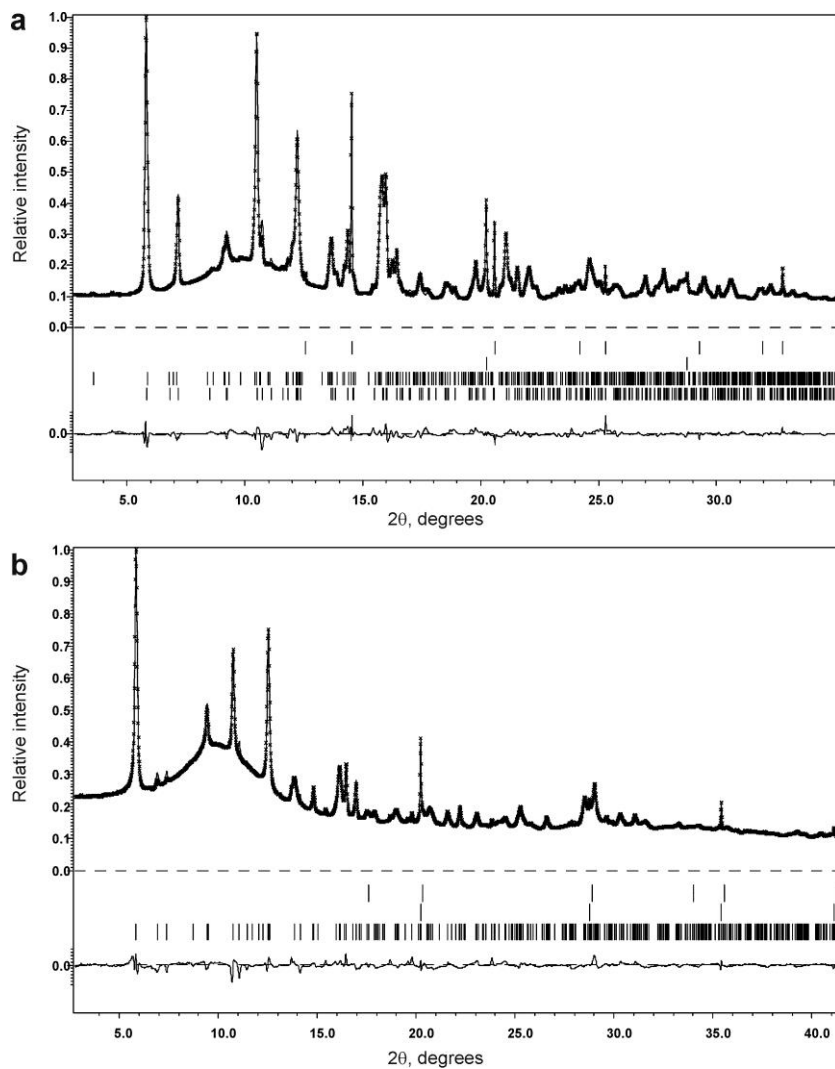


Figure S4. Experimental, calculated and difference SXPD profiles after the Rietveld refinement of NaFePO_4F (a) and $\text{Li}_{0.72}\text{Na}_{0.28}\text{FePO}_4\text{F}$ (b). The bars mark the reflection positions (a: NaFePO_4F (bottom row), $\text{Na}_{1.55}\text{FePO}_4\text{F}$ (37.1 wt.%, second row), Fe (1.4 wt.%, third row) and NaCl (7.0 wt.%, top row); b: $\text{Li}_{0.72}\text{Na}_{0.28}\text{FePO}_4\text{F}$ (bottom row), Fe (1.6 wt.%, middle row), Al (2.7 wt.%, top row)).

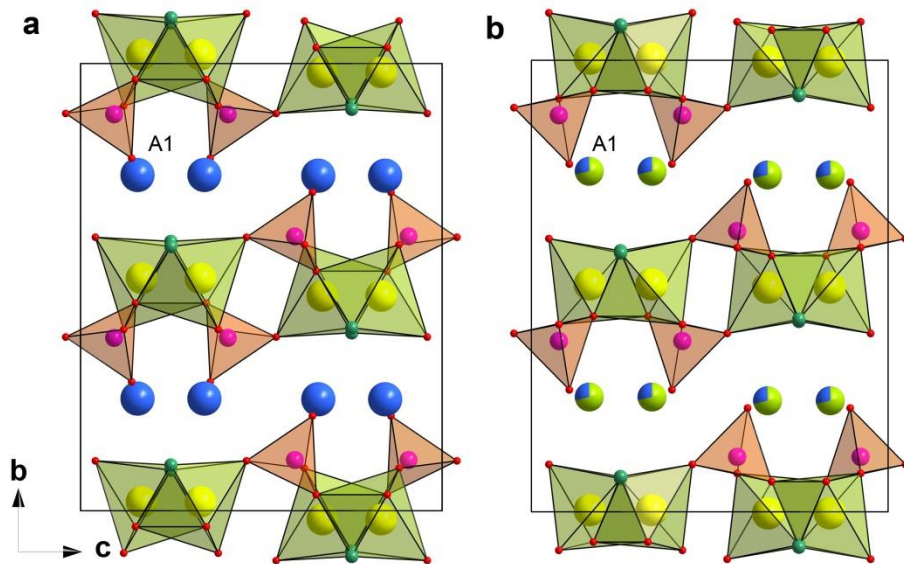


Figure S5. The crystal structures of the fully charged materials NaFePO_4F (a) and $\text{Li}_{0.72}\text{Na}_{0.28}\text{FePO}_4\text{F}$ (b). The Fe atoms are shown as dark green/yellow spheres, P atoms – as purple spheres, O and F atoms – as small red and green spheres, respectively. The A positions demonstrate their actual occupancy with Na (blue) and Li (light green), the occupancy factor is proportional to the size of the sectors.

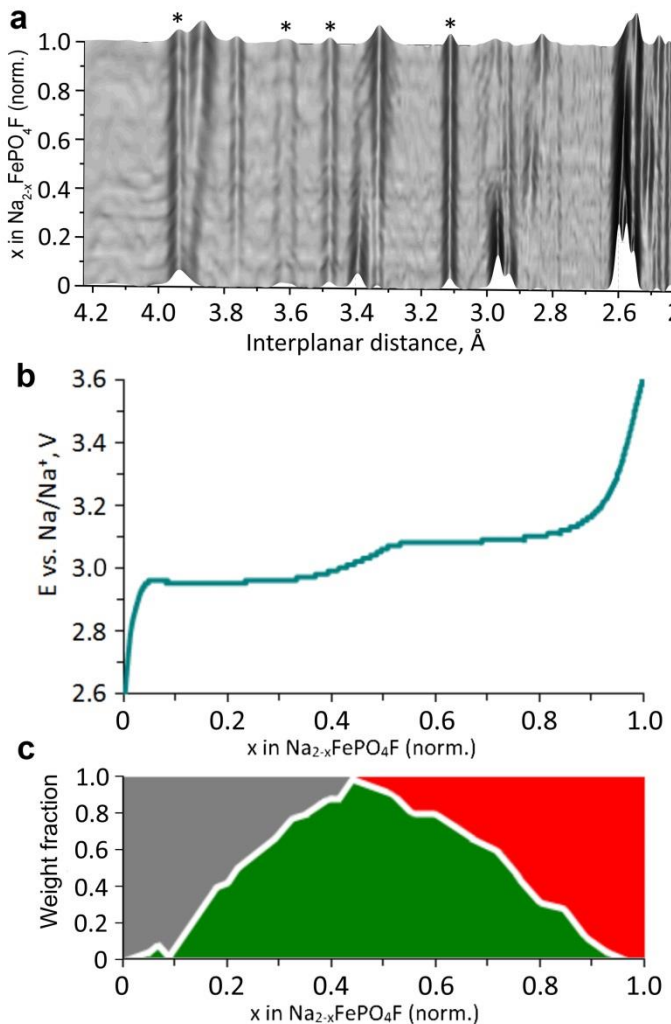


Figure S6. *Operando* PXRD patterns obtained in a Na-ion half-cell. By the asterisk are marked peaks of the components of the electrochemical half-cell besides the cathode material. Galvanostatic curve registered in the Na-ion half-cell at current density C/10 with *operando* collection of PXRD data (up) and the diagram demonstrating the accompanying composition evolution obtained from the Rietveld refinement (down): grey colour is for $\text{Na}_2\text{FePO}_4\text{F}$, green is for $\text{Na}_{1.55}\text{FePO}_4\text{F}$ and red is for NaFePO_4F ; the patterns are drawn in figure SX.

Table S12. Experimental unit cell parameters of $\text{Na}_2\text{FePO}_4\text{F}$ charged in the Na-ion and Li-ion cells in comparison to the DFT+ U GGA PBE and LDA calculated values ($\text{X} = \text{FePO}_4\text{F}$). The number in parenthesis in second column gives relative phase stability for similar compositions but different cation arrangements. For Na compounds GGA PBE overestimates lattice constants by <1%. For Li compounds the GGA PBE overestimates a and c constants by <2.5%, while b constant, which is highly sensitive to composition, is underestimated by 2% due to the mismatch of cation arrangement between theory and experiment. For charged in Li-ion cell cathode the LDA predicts a and c constants in perfect agreement with experiment. Since GGA PBE favors structures with larger volumes, the $\square\text{LiX}$ (Li in A2) with high volume (887 \AA^3) is slightly preferred by 0.01 eV/atom compared to $\text{Li}\square\text{X}$ (Li in A1) (764 \AA^3), contradicting to experimental results for $\text{Li}_{0.72}\text{Na}_{0.28}\text{FePO}_4\text{F}$, where Li resides in A1. The LDA predicts $\text{Li}\square\text{X}$ as a more stable phase (by 0.07 eV/atom) in agreement to experiment. The cation arrangements are provided in main text. The symbol \square stands for cation vacancy.

Sample	Composition, method, (phase stability, eV/at)	Space group	$a, \text{\AA}$	$b, \text{\AA}$	$c, \text{\AA}$	$\alpha, \text{deg.}$	$V, \text{\AA}^3$
Initial	Na_2X , Exp	$Pbcn$	5.2043(2)	13.7998(7)	11.8170(5)	90	848.7(5)
	Na_2X , GGA	$Pbcn$	5.25	13.95	11.90	90	871.2
Half-charged in Na-ion cell	$\text{Na}_{1.55}\text{X}$, Exp	$P2_1/b$	5.2039(4)	13.9115(9)	11.5377(8)	91.275(3)	835.1(1)
	$\text{Na}(\text{Na}_{0.5}\square_{0.5})\text{X}$, GGA	$P2_1/b$	5.22	14.03	11.70	91.2	857.3
Charged in Na-ion cell	NaX , Exp	$Pbcn$	5.1288(4)	14.085(1)	11.4041(8)	90	823.8(1)
	$\text{Na}\square\text{X}$, GGA, (0)	$Pbcn$	5.16	14.10	11.54	90	838.8
	$\square\text{NaX}$, GGA, (+0.026)	$Pbcn$	5.26	14.90	11.71	90	918.1
Half-charged in Li-ion cell	$\text{Na}_{0.73}\text{Li}_{0.88}\text{X}$, Exp	$Pbcn$	5.0137(4)	13.904(1)	11.1839(7)	90	779.6(1)
	$(\text{Na}_{0.5}\square_{0.5})\text{LiX}$, GGA	$P2_1/b$	5.15	13.82	11.61	91.2	825.4
	NaLiX , GGA, (0)	$Pbcn$	5.13	13.64	11.69	90	818.6
	LiNaX , GGA, (+0.006)	$Pbcn$	5.20	13.50	11.60	90	814.6
Charged in Li-ion cell	$\text{Li}_{0.72}\text{Na}_{0.28}\text{X}$, Exp	$Pbcn$	4.9714(5)	13.971(2)	11.047(1)	90	767.3(2)
	$(\text{Li}_{0.75}\text{Na}_{0.25})\square\text{X}$, GGA	Pc	5.09	13.69	11.31	90.1	788.1
	$(\text{Li}_{0.75}\text{Na}_{0.25})\square\text{X}$, LDA	Pc	4.97	13.21	11.07	90.2	727.0
	$\text{Li}\square\text{X}$, GGA, (+0.01)	$Pbcn$	5.09	13.28	11.31	90	763.9
	$\square\text{LiX}$, GGA, (0)	$Pbcn$	5.23	14.62	11.60	90	886.5

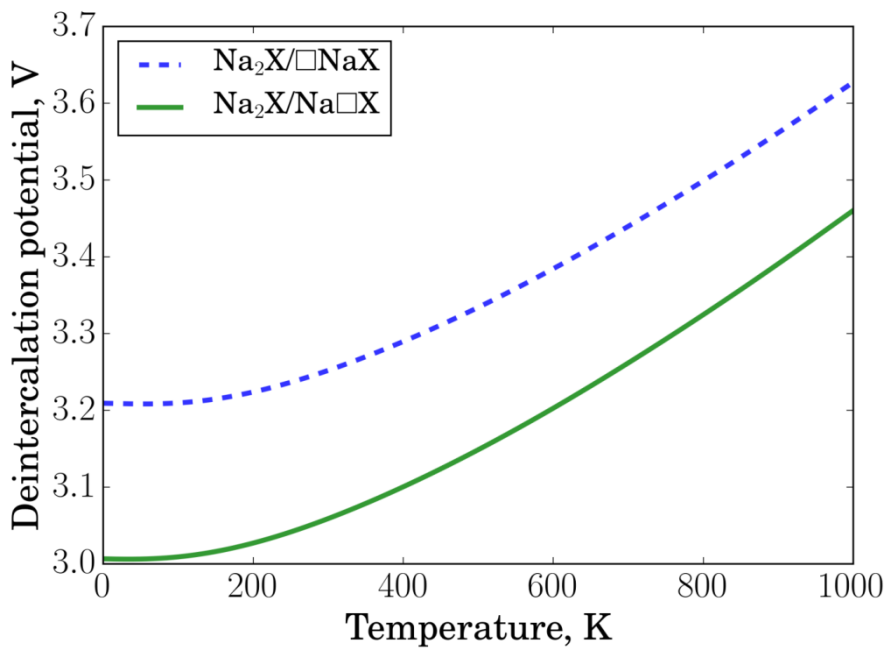


Figure S7. Temperature dependence of deintercalation potentials for $\square\text{NaFePO}_4\text{F}/\text{Na}_2\text{FePO}_4\text{F}$ (\square - cation vacancy) and $\text{Na}\square\text{FePO}_4\text{F}/\text{Na}_2\text{FePO}_4\text{F}$ couples corresponding to Na extraction from A1 and A2 positions, respectively. The corresponding free energies, required for the potential derivation, were obtained from DFT+*U* phonon calculations. The symbol \square stands for cation vacancy.

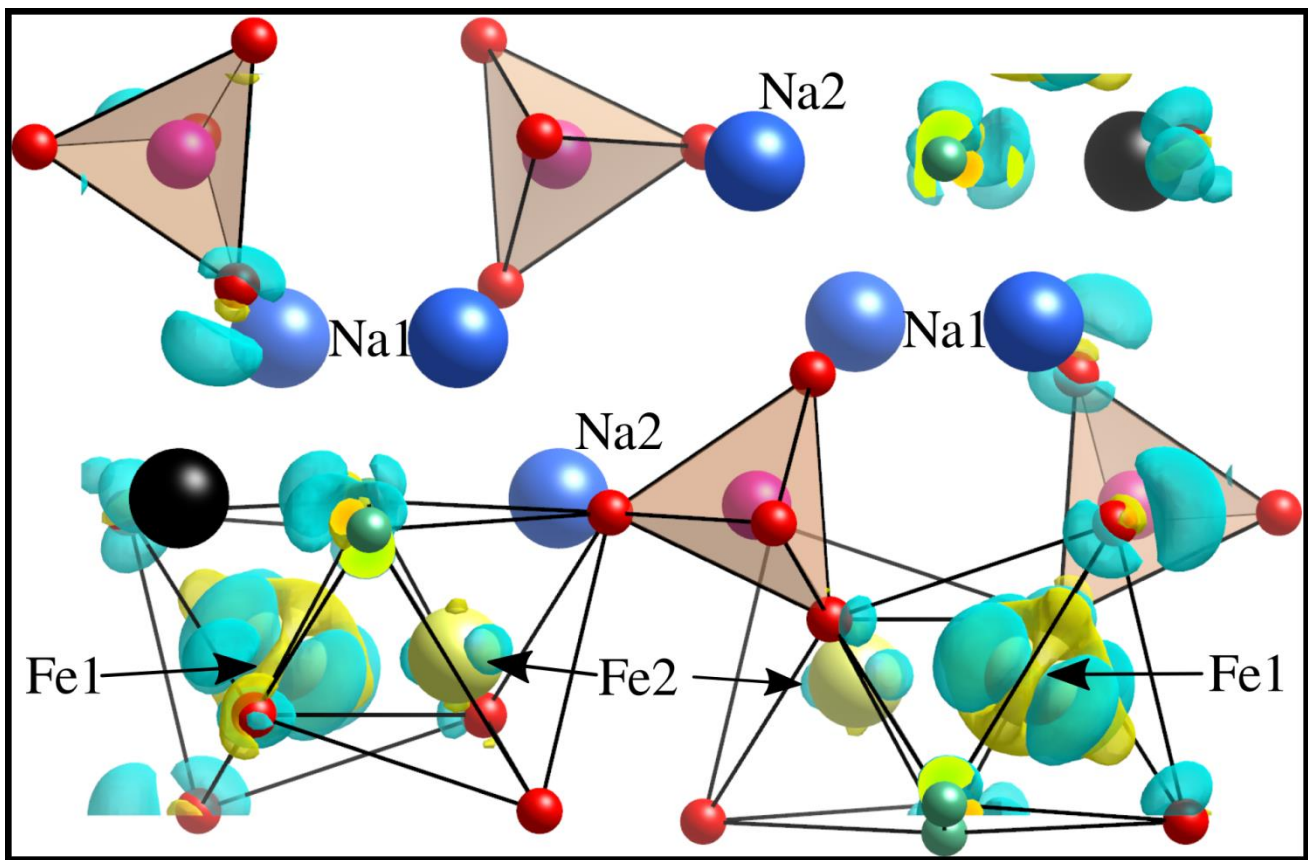


Figure S8. Charge density difference between $\text{Na}_{1.5}\text{FePO}_4\text{F}$ and $\text{Na}_2\text{FePO}_4\text{F}$. The positions of removed Na atoms are shown with black spheres. After extraction of the 1/4 of Na atoms the charge density is redistributed from oxygen atoms to iron atoms. It can be seen that pronounced charge redistribution occurs only on Fe1 atoms. The electrons are removed from t_{2g} band of Fe, which forms π bonds pointing in directions between oxygen ions. At the same time electrons accumulate at e_g^b band of Fe, which forms σ bonds between Fe and O, resulting in less ionic and more covalent bonds. The isosurface level is 0.005.